Whitlow W.L. Au
Arthur N. Popper
Richard R. Fay
Editors

Hearing by Whales and Dolphins

With 152 Illustrations

Springer

10
Acoustic Models of Sound Production and Propagation

JAMES L. AROYAN, MARK A. MCDONALD, SPAIN C. WEBB, JOHN A. HILDEBRAND, DAVID CLARK, JEFFREY T. LAITMAN, and JOY S. REIDENBERG

1. Introduction

Acoustic models based on physics and mathematics may yield significant advances in the understanding of sound production, propagation, and interaction associated with whales and dolphins. Models can be used to estimate the limits of intensity and frequency that are physically possible given the anatomy of a species. Models can also tell us what kind of anatomical structures would be necessary in order to produce sound having specific characteristics. Models can be used to clarify what type of measurements should be performed to answer specific questions. Many areas of bioacoustics stand to benefit from simulation of sound propagation through biological tissues and the media surrounding them. However, accurate modeling of biological subjects with complex anatomical features is extremely challenging, and few modern studies exist of sound production and propagation in whales and dolphins.

In this chapter, we will consider two acoustic models, the first dealing with the propagation of echolocation signals through the head of a dolphin. This model combines a novel tissue modeling approach with techniques of numerical wave propagation to study the acoustic principles operating in the biosonar emission and reception processes. The second model deals with the production of low-frequency sounds by the blue whale, *Balaenoptera musculus*. The features of blue whale sounds are considered and a sound production mechanism is derived taking the structures of the whale's anatomy into account along with the physics of acoustics. The first model results from the research of Aroyan (1996) and the second model is the result of research by the remaining authors.

2. Three-Dimensional Numerical Simulation of Biosonar Emission in the Common Dolphin

Measurements of the acoustic field of echolocating dolphins have demonstrated that dolphins emit a rapid series of intense pulses in a narrowly focused beam that emanates from the forehead and rostrum. Despite application of a variety of experimental techniques, the exact mechanisms involved in the generation, emission, and reception of delphinid biosonar signals have remained conjectural. Advances in the methodology of bioacoustic simulations have led to powerful combinations of techniques capable of addressing questions that have proven difficult to resolve experimentally. Aroyan (1996) combined methods for three-dimensional (3-D) acoustic simulation and far-field extrapolation with a novel approach to the mapping of acoustic tissue parameters from X-ray computed tomographic (CT) data. These techniques, applied to models of the forehead and lower jaw tissues of the common dolphin, *Delphinus delphis*, enabled a detailed study of the patterns of sound propagation within the modeled tissues and, hence, of the acoustic principles operating in the biosonar emission and reception processes. The following sections discuss the methods used in this investigation and present a series of results concerning the location of the biosonar signal source tissues, the roles of the skull, air sacs, and soft tissues (including the melon) in beam formation, and the acoustical consequences of forehead asymmetry in *Delphinus delphis*.

2.1 Computational Methods

The following approach was used to investigate the *D. delphis* emission system. First, computer models of the tissues of the dolphin's head were constructed using a novel mapping of both tissue density and acoustic velocity from X-ray CT attenuation data to a simulation grid. Second, 3-D finite difference programs were used to simulate acoustic propagation into the tissue models to locate the source region of the dolphin's biosonar emissions (analogous to the use of inverse seismologic simulations to pinpoint the underground source point or "hypocenter" of an earthquake, or to reversing the emission/collection role of an optical lens system). Third, sources were placed at these inverse simulation "hypocenters" or at conjectured anatomical source locations, and finite difference programs were again used to propagate the acoustic field of the source and tissue models out to a surface surrounding the tissue region of the grid. Fourth, boundary extrapolation programs were used to compute the emitted acoustic far-field from the pressure and its normal derivative over this surface. Biosonar mechanisms were investigated by visualizing the acoustic energy density within a variety of tissue models and by comparing the fields emitted by these models to the experimentally measured sonar emissions of live animals. Conceptually, this approach involves: (1) contructing the best pos-

sible acoustical model of the dolphin's tissues from the available data; (2) utilizing the reversibility of wave propagation to let the model tell us what its focal characteristics are; and (3) applying the resulting focal information in forward simulations to determine the emission properties for each model. Each step of this procedure has yielded new insights into the acoustic mechanisms of delphinid biosonar.

In order to study the patterns of sound propagation within the forehead tissues, propagation through tissue models was simulated by numerical integration of the acoustic wave equation. Shear wave velocities for soft tissues remain less than 1% of the compressional wave sound speed for frequencies below 1 MHz, and soft tissue shear wave attenuation coefficients are of the order of 10^4 times the compressional wave attenuation coefficients (Frizzell et al., 1976; Carstensen 1979; Madsen, et al., 1983). Additionally, the fact that air sacs normally cover much of the skull surface in the vicinity of the nasal passages in delphinids also suggests that shear modes do not play a significant role in biosonar emissions. In the current simulations, tissues (including bone) were modeled as inhomogeneous fluids and shear wave modes were ignored.

In fluids of inhomogeneous density and velocity, the linearized wave equation for acoustic pressure p is (Pierce 1981; Aroyan 1990):

$$\frac{1}{c^2(\mathbf{x})}\frac{\partial^2 p}{\partial t^2} = \nabla^2 p - \frac{\nabla p \cdot \nabla \rho(\mathbf{x})}{\rho(\mathbf{x})} \tag{1a}$$

Both the sound speed c and density ρ are functions of position $\mathbf{x}$, while the acoustic pressure p is dependent on position and time, $p = p(\mathbf{x}, t)$. By mapping the values of tissue velocity and density onto a grid, finite differencing schemes can be used to propagate the solution of Eq. 1a forward in time. The following discretization of Eq. 1a, solved for the numerical value of the acoustic pressure $P^{m+1}_{i,j,k}$ at grid position (i, j, k) and time step $(m + 1)$, was applied over the tissue region of the grid:

$$\begin{aligned}
P^{m+1}_{i,j,k} &= (2 - 7.5\kappa^2_{i,j,k})P^m_{i,j,k} - P^{m-1}_{i,j,k} \\
&+ \frac{4\kappa^2_{i,j,k}}{3}[P^m_{i+1,j,k} + P^m_{i-1,j,k} + P^m_{i,j+1,k} + P^m_{i,j-1,k} + P^m_{i,j,k+1} + P^m_{i,j,k-1}] \\
&- \frac{\kappa^2_{i,j,k}}{12}[P^m_{i+2,j,k} + P^m_{i-2,j,k} + P^m_{i,j+2,k} + P^m_{i,j-2,k} + P^m_{i,j,k+2} + P^m_{i,j,k-2}] \\
&- \frac{\kappa^2_{i,j,k}}{3\rho_{i,j,k}}[(P^m_{i+1,j,k} - P^m_{i-1,j,k}) - (P^m_{i+2,j,k} + P^m_{i-2,j,k})/8](\rho_{i+1,j,k} - \rho_{i-1,j,k}) \\
&- \frac{\kappa^2_{i,j,k}}{3\rho_{i,j,k}}[(P^m_{i,j+1,k} - P^m_{i,j-1,k}) - (P^m_{i,j+2,k} + P^m_{i,j-2,k})/8](\rho_{i,j+1,k} - \rho_{i,j-1,k}) \\
&- \frac{\kappa^2_{i,j,k}}{3\rho_{i,j,k}}[(P^m_{i,j,k+1} - P^m_{i,j,k-1}) - (P^m_{i,j,k+2} + P^m_{i,j,k-2})/8](\rho_{i,j,k+1} - \rho_{i,j,k-1})
\end{aligned} \tag{1b}$$

In this equation, $\kappa_{i,j,k} = (l/h)c_{i,j,k}$ is a nondimensionalized version of the spatially varying acoustic velocity $c_{i,j,k}$; $\rho_{i,j,k}$ is the spatially varying density; and $l = \Delta t$ and $h = \Delta x = \Delta y = \Delta z$ are the temporal and spatial grid increments, respectively. This scheme is fourth order in the spatial derivatives of pressure, second order in the spatial derivatives of density, and second order in the time derivative of pressure. The first three lines of Eq. 1b constitute the scheme for the homogeneous wave equation. This homogeneous scheme was used outside the tissue regions of the grid and greater than two points away from the grid edges. A second order spatial derivative scheme was applied at the next-to-last grid points. Absorbing boundary conditions were applied at the extreme grid edges to reduce reflections from grid boundaries to very low levels.

Figure 10.1a illustrates a typical simulation grid layout. The region of the grid containing the tissue model is indicated. Except for a few trials on half-resolution grids, a 1.5-mm cubic grid corresponding to the finest X-ray CT data voxel size was used in the forehead simulations. For the inverse simulations, the front face of the grid was used as a flat source to ensonify the tissue model region with a cosine-windowed "echo" at a fixed frequency and angle of return. A windowed aperture function was used to reduce the near-field diffraction of this source. The energy density at the focal maxima found in the inverse simulations were two to three orders of magnitude above variations caused by near-field diffraction and uneven ensonification of the model region.

Several different quantities may be calculated from the simulated pressure field and visualized with graphics packages in order to illustrate the patterns of sound propagation within the tissue models. For example, one may visualize the time-averaged magnitude of the total acoustic energy density W_{total} as the sum of the potential acoustic energy density $W_{\text{potential}}$ and the kinetic acoustic energy density W_{kinetic} (Pierce 1981; Morse and Ingard 1968)

$$W_{total} = W_{potential} + W_{kinetic} = \frac{1}{2\rho c^2}[\mathrm{Re}(p)]^2 + \frac{\rho}{2}|\mathrm{Re}(\mathbf{u})|^2 \qquad (2)$$

where the vector fluid velocity $\mathbf{u} = \nabla p/(i\omega\rho)$. Alternatively, one may visualize the time-averaged magnitude of the potential energy density $W_{\text{potential}} = [\mathrm{Re}(p)]^2/(2\rho c^2)$, as in Aroyan (1996). In this chapter, we will visualize either the total or the potential acoustic energy density, although all three forms of energy density (potential, kinetic, or total) and/or the acoustic intensity vector yield significant information regarding propagation within tissues.

In order to compute the emitted far-field patterns of various source and tissue models, the simulated pressure field and its normal derivative over a rectangular surface immediately surrounding the tissue region of the grid was used as input to boundary integral extrapolation programs. The

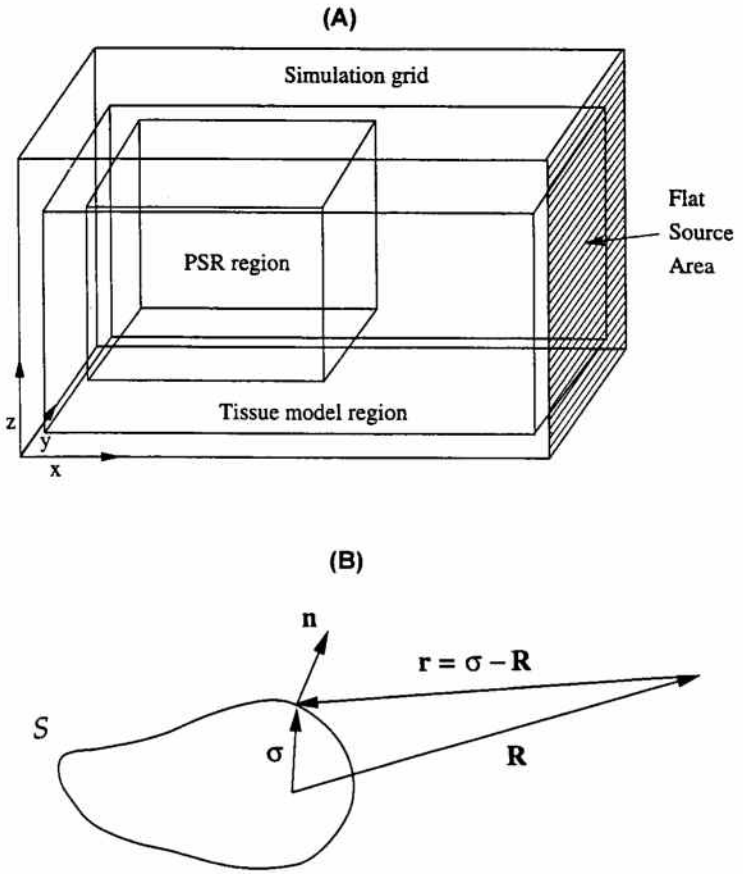

FIGURE 10.1. (A) Typical simulation grid layout. All inverse simulations used the front face of the grid as a flat source to ensonify the tissue region with "echoes" at various angles of return. In the inverse forehead simulations, the acoustic energy density within the subvolume labeled "PSR" was visualized. In all forward simulations, the pressure and its normal derivative over a surface immediately surrounding the source and tissue model were used to compute the far-field emission patterns. (B) Diagram of the geometry assumed by Eq. 3. Field points **R** are assumed to lie in the sourceless and homogeneous region exterior to the extrapolation surface S, which encloses an arbitrary source volume.

Helmholtz integral equation relates the pressure p and the normal derivative of the pressure $\partial p/\partial n$ over a surface S surrounding an arbitrary distribution of sources to the pressure $p(\mathbf{R})$ produced by those sources at any field point **R** (Baker and Copson 1953; Copley 1968; Schenck 1968). The geometry assumed here is illustrated in Figure 10.1b. For

points **R** lying exterior to the source volume enclosed by surface S, the Helmholtz integral equation has the form (Junger and Feit 1986; Aroyan 1996)

$$p(\mathbf{R}) = -\oint_S \left\{ p(\boldsymbol{\sigma}) \frac{\partial G(\boldsymbol{\sigma},\mathbf{R})}{\partial n} - G(\boldsymbol{\sigma},\mathbf{R}) \frac{\partial p(\boldsymbol{\sigma})}{\partial n} \right\} dS(\boldsymbol{\sigma}) \tag{3}$$

Here $\boldsymbol{\sigma}$ defines the vector coordinates of surface S, while $\partial/\partial n = \mathbf{n} \cdot \nabla$ denotes the directional derivative along the outward pointing unit vector **n** normal to surface S. We have also used the notation $G(\boldsymbol{\sigma}, \mathbf{R})$ for the 3-D free-space Green's function,

$$G(\boldsymbol{\sigma},\mathbf{R}) = -\frac{e^{ik|\boldsymbol{\sigma}-\mathbf{R}|}}{4\pi|\boldsymbol{\sigma}-\mathbf{R}|} = -\frac{e^{ikr}}{4\pi r}, \quad \mathbf{r} = \boldsymbol{\sigma} - \mathbf{R}, \tag{4}$$

where $k = \omega/c$ is the acoustic wave number, ω is the angular frequency of the field, and c is the (constant) speed of sound propagation at surface S and in the medium external to S. No assumptions are made about the distribution of sound sources, speeds, or other properties of materials inside surface S—this source region may be arbitrarily complex. In addition, S may be any closed surface surrounding the source region. The medium external to S, however, is assumed to be infinite, homogeneous, and sourceless. Because the extrapolation surface S can be located immediately outside the tissue model region of the simulation grid, an enormous reduction of the grid size required for far-field calculation is realized. In the current bioacoustic application, a far-field form of Eq. 3 was utilized: Appendix A gives this far-field formulation and notes aspects of its numerical implementation. Appendix A also provides an example of a simple computed far-field pattern and introduces an efficient representation of this data over all emission directions, which is used in all emission diagrams of Section 3.

2.2 *Model of the Dolphin*

This section outlines a new approach to modeling the acoustic parameters of delphinid soft tissues from X-ray CT attenuation data. This method generates approximations of the 3-D density and velocity distributions within scanned delphinid tissues that agree well with reported measurements.

An X-ray CT scan of the head of a male (body length = 1.92 m) common dolphin, *D. delphis*, was provided by Dr. Ted W. Cranford (identified as speciment D4 in Cranford et al. 1996). The spacing of the scan planes in the original CT data set varied from 5.0 mm over the rostrum, to 1.5 mm over the narial region, to 3.0 mm over the posterior cranium. Individual scans consisted of 320 × 320 pixel transverse sectional images on a 1.5-mm square grid. For simulation purposes, the tissue region of the original data was linearly interpolated in the x-direction to planes uniformly spaced 1.5 mm apart. The resulting data set was then used either at full resolution

(on a 1.5-mm cubic grid) or half resolution (on a 3.0-mm cubic grid).

For the GE CT9800 scanner used to collect the *D. delphis* data, a linear mapping between X-ray attenuation values in Hounsfield Units (HU) and human tissue density has been shown to be accurate to within ±5% for densities ranging from soft tissue to cortical bone (Henson, Ackland, and Fox 1987). The slope of this correspondence varies with the beam energy of the scanner. Application of more precise medical techniques for tissue HU-to-density mapping could potentially reduce these errors to well below 1% (Erlichman 1986; Cann 1988; Hunter 1988). The present study assumed that the scan image pixel values were linearly related to Hounsfield Units, and mapped tissue densities from HU values using the linear model shown in Figure 10.2a. Three calibration points confirming this map were provided by the known density (0.90 g/cc) of the inner melon (Varanasi et al. 1975), the known density (1.18 g/cc) of the plexiglass specimen registration frame, and the maximum density (roughly 2.7 g/cc) of delphinid periotic bone (Lees et al. 1996). The image scale ranges from −1,024 to +2,519 HU. The low end of the scale (below −138 HU) was below all soft tissue structures (except air sacs, which were handled separately). Since it was necessary to map the air surrounding the scanned specimen to seawater, this lower range is mapped to the density of seawater (1.03 g/cc) in Figure 10.2a.

Tissue velocity was then deduced from the above tissue density information and the following experimental data. Figure 10.2b plots average experimental density and velocity values and approximate ranges for several types of normal (fresh) terrestrial mammalian soft tissues and delphinid melon lipids at 37°C from literature sources. Terrestrial mammalian tissue data was taken from Parry and Chivers (1979), Goss et al. (1980), Lele and Sleefe (1985), and Miles (1996). Bottlenose dolphin melon lipid velocity data was taken primarily from Norris and Harvey (1974) and secondarily from Litchfield et al. (1979), since the latter study measured the velocities of lipid samples after extraction from melon and blubber tissues. Extraction of the lipids from connective tissue components probably lowered the values reported for the velocities of the "outer" and "under" melon. Both papers agree approximately on the velocity range for the inner melon tissues. Melon and lower jaw lipid densities (down to .90 g/cc) are taken from Varanasi, Feldman, and Malins (1975) assuming a 60% to 40% by weight triglyceride-isovalerate wax ester melon lipid composition, which is similar across the family Delphinidae (Litchfield et al. 1975). Although few measurements of intact tissue velocity, density, and temperature are available, an attempt was made to define the ranges for the normal mammalian tissues in Figure 10.2b as 1-sigma deviations in the tabulated values. The density and velocity ranges for delphinid melon lipids shown in Figure 10.2b correspond to the ranges that exist within the layered melon tissues.

It is important to note that the velocity of terrestrial mammalian soft tissues is correlated approximately linearly with density in the range from

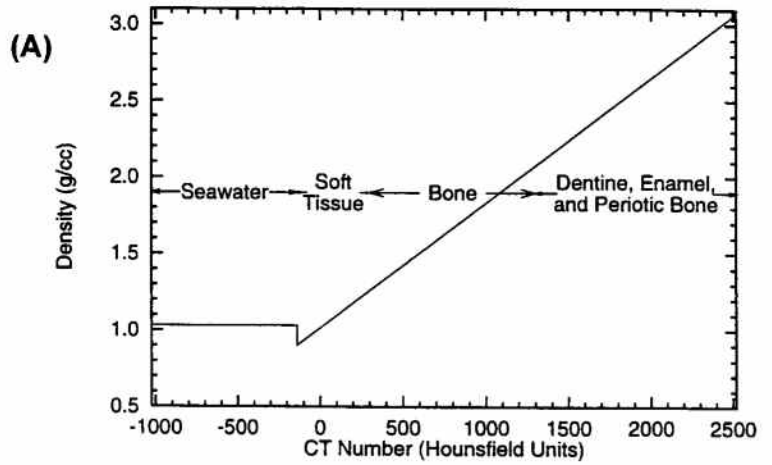
(A)
Density (g/cc)
3.0
2.5
2.0
1.5
1.0
0.5
Seawater
Soft Tissue
Bone
Dentine, Enamel, and Periotic Bone
-1000
-500
0
500
1000
1500
2000
2500
CT Number (Hounsfield Units)

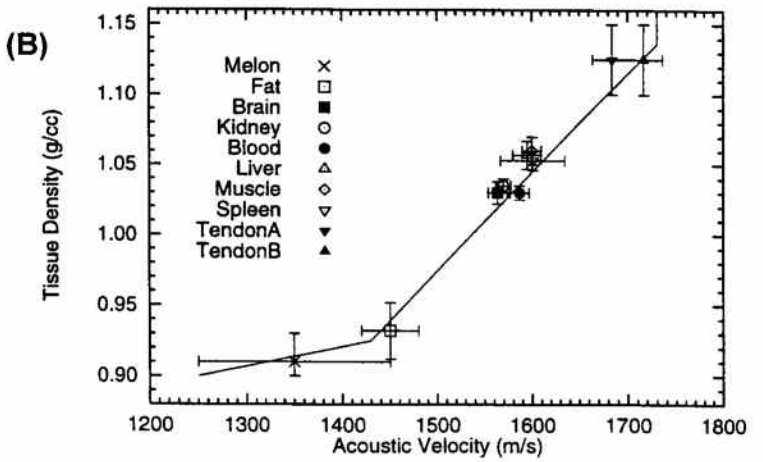
(B)
Tissue Density (g/cc)
1.15
1.10
1.05
1.00
0.95
0.90
Melon
Fat
Brain
Kidney
Blood
Liver
Muscle
Spleen
TendonA
TendonB
1200
1300
1400
1500
1600
1700
1800
Acoustic Velocity (m/s)

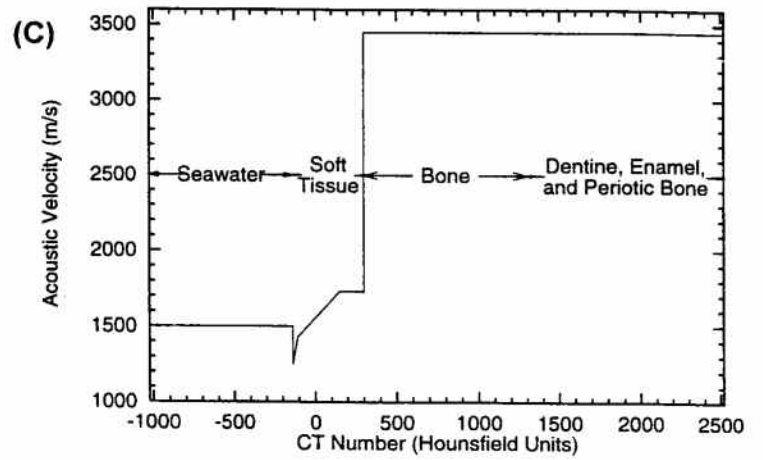
(C)
Acoustic Velocity (m/s)
3500
3000
2500
2000
1500
1000
Seawater
Soft Tissue
Bone
Dentine, Enamel, and Periotic Bone
-1000
-500
0
500
1000
1500
2000
2500
CT Number (Hounsfield Units)

normal fat to tendon. The lipids of the delphinid melon and lower jaw are, however, chemically and acoustically distinct from other body fats and blubber (Litchfield et al. 1973; Litchfield et al. 1975, 1979; Malins and Varanasi 1975; Varanasi et al. 1975; Varanasi et al. 1982). It therefore makes sense to correlate the velocities of all soft tissues except the melon and lower jaw fats with their densities using a linear mapping from ordinary fat to tendon for the characteristic mammalian soft tissue range. The unique "acoustic fats" can then be incorporated by adding an extension from normal fat down to the lower melon lipid density and velocity threshold. Given the magnitude of the variations in mammalian soft tissue densities and velocities, a two part linear mapping was deemed satisfactory for the series of simulations reported here. The acoustic phenomena of interest to this study result mainly from relatively short propagation paths (10 wavelengths or less) through dermal layers, blubber, melon fat, muscle, and connective tissues. Because biologically reasonable variation of the velocity mapping did not produce significantly different results, the velocities of these tissues was presumed to be adequately represented by the current model. This piecewise linear mapping of density versus velocity for the soft tissue range is indicated by the solid line in Figure 10.2b, demonstrating that a good correspondence can be achieved between soft tissue velocity and density. The current study is the first to have approximated the 3-D density and velocity structures of all soft tissues including the melon and lower jaw fats and to have accurately simulated 3-D acoustic propagation within those structures. Diagrams of the resulting tissue density, velocity, and impedance structure in a right parasagittal section through the core of the *D. delphis* melon can be found in Aroyan (1996). Previous analytical and ray tracing studies had assumed highly simplified two-dimensional tissue density and/or velocity models. (Compare, for example, Evans et al. 1964; Dubrovskiy and Zaslavskiy 1975; Litchfield et al. 1979; Aroyan et al. 1992; Au 1993).

Because the HU-to-density map has already been specified (Figure 10.2a), the empirical density-to-velocity map (Figure 10.2b) then determines the soft tissue HU-to-velocity mapping. The HU-to-velocity mapping

FIGURE 10.2. (A) Plot of the linear mapping from CT values (in Hounsfield Units) to tissue density used in the simulations. Tissue types corresponding to mapped CT ranges have been indicated. (B) Plot of approximate values and ranges of density and velocity for several types of normal terrestrial mammalian soft tissues and delphinid melon lipids measured at 37°C. Tendon A refers to propagation perpendicular to the tendon fiber bundles. Tendon B refers to propagation along the tendon fiber axis. The solid line indicates the piecewise linear mapping of density to velocity used in the simulations over the range of soft tissues. (C) Plot of the mapping from CT values (in Hounsfield Units) to tissue velocity used in the simulations. This mapping (over the soft tissue range) is implied by the upper two figures. Tissue types corresponding to mapped CT ranges have been indicated.

used in this study is pictured in Figure 10.2c. The soft tissue range of this mapping generates good agreement between Cranford's (1992) plots of HU values through a *Tursiops truncatus* melon and Norris and Harvey's (1974) *T. truncatus* melon velocity measurements. While intact tissue velocities for *D. delphis* have not been measured, it is reasonable to expect that a mapping based on the measured acoustic properties of mammalian tissues and that appears to work for *T. truncatus* will work for other delphinids as well, provided the data ranges for each specimen have been properly determined. Similar triglyceride and isovalerate wax ester lipid mixtures (roughly 60% and 40% composition by weight, respectively) are found in the melon and lower jaw fats across the family Delphinidae (Litchfield et al. 1975). These ratios differ substantially from blubber compositions. Slight variations of the delphinid lipid density and velocity mapping presented here should be sufficient for modeling the odontocete families Phocoenidae and Monodontidae. The families Platanistidae, Ziphiidae, and Physeteridae, however, may require different treatments.

Several aspects of Figure 10.2c merit mention. First, the attenuation range below –138 HU (below all soft tissue structures except air sacs) is again assigned the velocity of seawater (1,500 m/s). Next, soft tissue velocities above tendon (at 150 HU) and up to the bone threshold (at 300 HU) are modeled as a constant 1,730 m/s. This was done because the data range 150 to 300 HU corresponded to the range of partial-volume blurring of the soft tissue–bone interface, and because measured soft tissue velocities do not appear to exceed this value. The "partial-volume" effect is one of several potential sources of error in X-ray CT data (Cann 1988). It occurs when a scanned volume element straddles a sharp tissue interface, effectively blurring the interface. A large discontinuity in velocity at the bone threshold was introduced to correct for the artifact of partial-volume blurring of the soft tissue–bone interface. We also mention that partial-volume blurring of the skin–seawater interface was corrected using a simple technique (Aroyan 1996, p 91), but that no correction was made in the current model for tissue velocity dependence on temperature near the skin of the animal. Finally, note that the velocity above the bone threshold was modeled as a constant 3,450 m/s. The threshold for bone at 300 HU was determined by examining the thickness and continuity of skull surfaces crucial to acoustic behavior. As in previous two-dimensional simulations (Aroyan 1990; Aroyan et al. 1992), the 3-D results are not strongly dependent on the exact acoustical parameters assigned to bone.

Modeling of air spaces within soft tissue introduces unique difficulties. While the geometry of skull–soft tissue and external soft tissue–air interfaces is generally well represented in high-resolution X-ray CT data, air sacs inside soft tissues can suffer distortion due to postmortem changes. Modeling of a dolphin's nasal passages is further complicated by the common observation that the uppermost nasal sacs in live animals are, to some extent, mobile during phonation (Dormer 1979). Therefore, the author

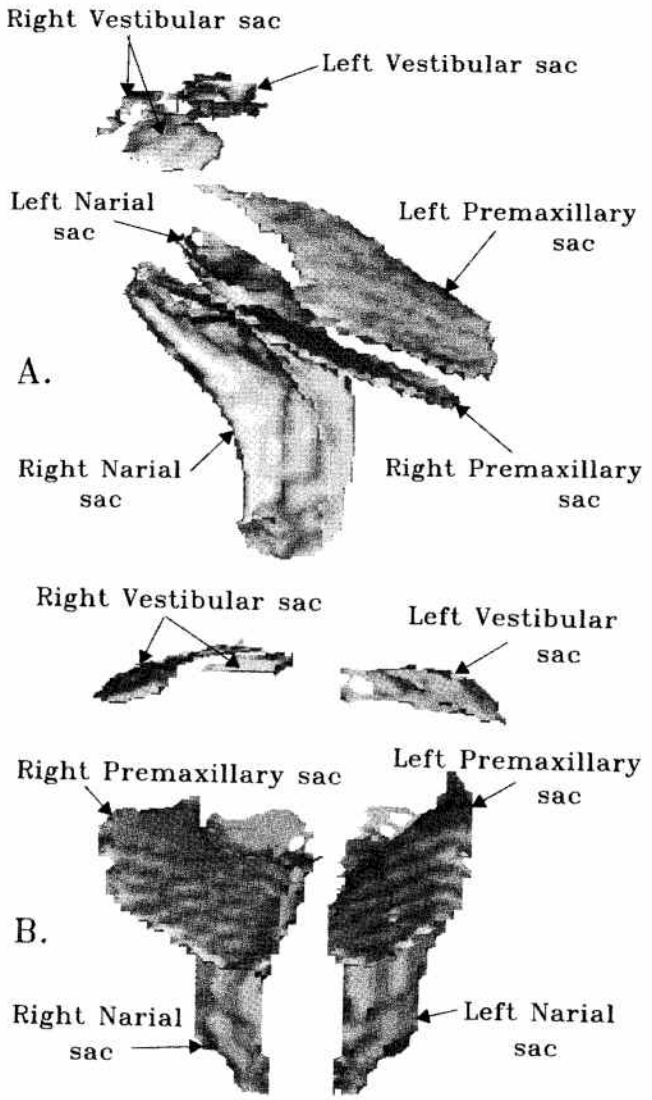

FIGURE 10.3. Visualizations of the model of the narial, vestibular, and premaxillary air sacs used in the simulations. Upper figure (A) is an elevated right-side view of the sac surfaces; lower figure (B) is an elevated front view. Labels identify the individual sacs included in the model.

chose the simplest model of the upper nasal sacs that was supported by the X-ray CT data and by previous anatomical studies.

Perspective views of this simplified air sac model are shown in Figure 10.3. Outlines of the narial air spaces were very clear in the *D. delphis* CT

data. The vestibular sacs, however, were only marginally discernable. By extracting all CT data coordinates with values below soft tissue thresholds, the narial sacs and portions of the vestibular sacs were located. Unfortunately, the inferior vestibule, the spiracular cavity, and the premaxillary, nasofrontal, and accessory sacs were not even marginally discernible in this data. Nevertheless, the location of the premaxillary sacs is so well documented in the literature that the author deemed it permissible to include their positions above the premaxillary shelves of the skull in the model (Mead 1972; Dormer 1979). Note that portions of both left and right vestibular sacs, as well as other sacs in their entirety, are missing from this model.

As in previously reported simulations (Aroyan 1990; Aroyan et al. 1992), air sacs were simulated as pressure release surfaces by setting the pressure to zero at all sac coordinates. Note that this procedure eliminates any potential air-cavity resonance behavior.

3. Results of the Simulations

To provide an overview of the acoustical focal behavior of the head of the common dolphin, consider first the result of ensonifying a full head model with a (cw) 50-kHz sound beam incident from directly forward of the animal. Figure 10.4a illustrates the skin isosurface of this full model, which incorportated the skull, soft tissues, upper nasal air sacs, the peribullar sinuses surrounding most of the inner ears, and the pterygoid sinuses of the lower skull and palate. The full head model utilized the entire CT data set at half resolution (mapped to a 3.0-mm cubic grid). Figure 10.4b illustrates an isosurface at 30% of the maximum total acoustic energy density W_{total} (Eq. (2)) within the same model volume (and perspective) illustrated in Figure 10.4a. Significantly, three bright focal points occur within the model, each with an associated "funnel" or "channel" of energy density leading up to it. Funnels occur within both left and right fat bodies of the lower jaw, which narrow back to create sharp maxima against the lateral surfaces of each respective (left and right) tympanoperiotic complex. This channeling behavior of the lower jaw fat bodies strongly improves the forward receptivity of the simulated hearing patterns of both left and right ears (Aroyan 1996). The thinner-at-the-center thickness profile of each (left and right) lower jaw pan bone surrounded by low-speed fat apparently acts as a "fast" lens structure contributing to the creation of distinct forward receptivity peaks for each ear. The peribullar sinuses were also found to be highly effective in shielding the ears from directions of incidence other than forward and downward. All three results suggest mechanisms potentially fundamental to lower jaw hearing by delphinid cetaceans (Norris 1968, 1980); however, project results concerning the biosonar reception process must

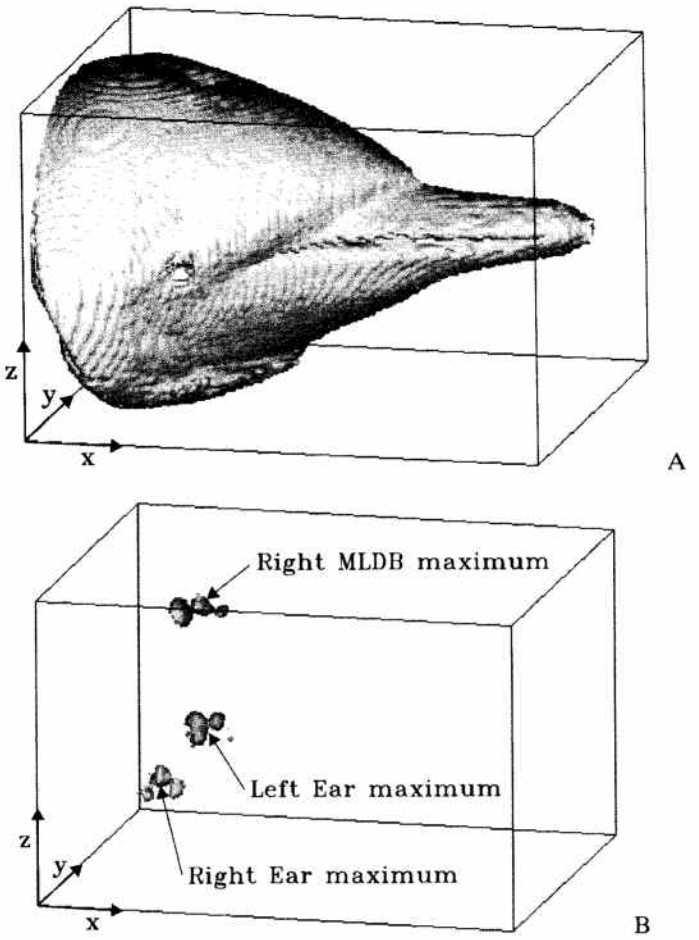

FIGURE 10.4. (A) Visualization of the skin isosurface of the full head model using the complete CT data set mapped to a 3.0-mm cubic grid. This rectangular model volume has x, y, z side-lengths of 44.7, 26.1 and 27.9 cm. (B) Illustration of an isosurface at 30% of the maximum total acoustic energy density W_{total} within the same tissue model volume (and perspective) illustrated in Figure 10.6 for a 50-kHz $(\theta, \phi) = (0°, 0°)$ inverse simulation (sound beam incident from straight ahead). The locations of the three bright focal maxima that occur within the model are labeled.

be discussed elsewhere. A funnel also occurs within the melon tissue of the forehead, which narrows back to create a bright maximum just below the right monkey lips-dorsal bursae (MLDB) complex (Cranford 1992; Cranford et al. 1996) within the soft tissue of the right nasal complex. This focal structure in the forehead and the locality of its maxima

recur over a range of ensonification directions for all frequencies tested and are quite robust with respect to biologically reasonable variation of the HU-to-density and HU-to-velocity model mappings discussed in Section 2.2.

We now proceed to examine in detail the focal behavior of the forehead tissues suggested by Figure 10.4b. Results of inverse and forward simulations are presented below for three different models of the forehead of the common dolphin: for a skull-only model, for a skull and soft tissues (including the melon) model, and for a complete skull, air sacs, and soft tissue model. We will also present the results of several moved source simulations using the complete model.

3.1 Skull-Only Simulations

The region of the CT data set selected for more detailed forehead simulations is illustrated by an isosurface at the CT data bone threshold (300 HU) in Figure 10.5a and by bone and skin isosurface in Figure 10.5b. This tissue region is a rectangular volume having x,y,z side-lengths of 27.0, 12.6, and 12.6 cm, represented on a 1.5-mm cubic grid. In the skull-only model, the HU-to-density and HU-to-velocity mappings of Section 2.2 were used to assign velocity and density values only to tissue coordinates with Hounsfield numbers equal to or greater than the bone threshold. All other model coordinates were mapped to background seawater density (1.03 g/cc) and velocity (1,500 m/s). The last few points of the density and velocity grids along the back, bottom, and side edges of the tissue region were graded back to seawater values in order to reduce spurious reflections at the model boundary.

The maxima of the inverse forehead simulations all occurred within a small volume of the supranarial region in all models. We will therefore illustrate the detailed inverse simulation data only within a subvolume of the forehead tissue model here referred to as the "potential source region" (PSR), which includes the supranarial region and extends forward to include about half of the melon body. The rectangular PSR volume (x,y,z side-lengths of 12.0, 9.0 and 9.0 cm) of the forehead model is outlined (boxed) in Figures 10.5a and b. To help establish positional reference with respect to the skull and soft tissue structures, Figure 10.5c illustrates a parasagittal slice through the center of the right MLDB complex within the PSR. Cranford et al. (1996) provide a review of relevant delphinid forehead tissue structures. The center of the left MLDB complex lies within the PSR, approximately 3.3 cm to the left and about 0.7 cm downward from the center of the right MLDB.

Figures 10.6a and b illustrate the acoustic potential energy density $W_{\text{potential}}$ in the PSR planes containing the maxima or "hypocenters" for skull-only inverse simulations at (cw) frequencies of 50 and 75 kHz, respectively. The direction of return propagation in this case was 5° below the

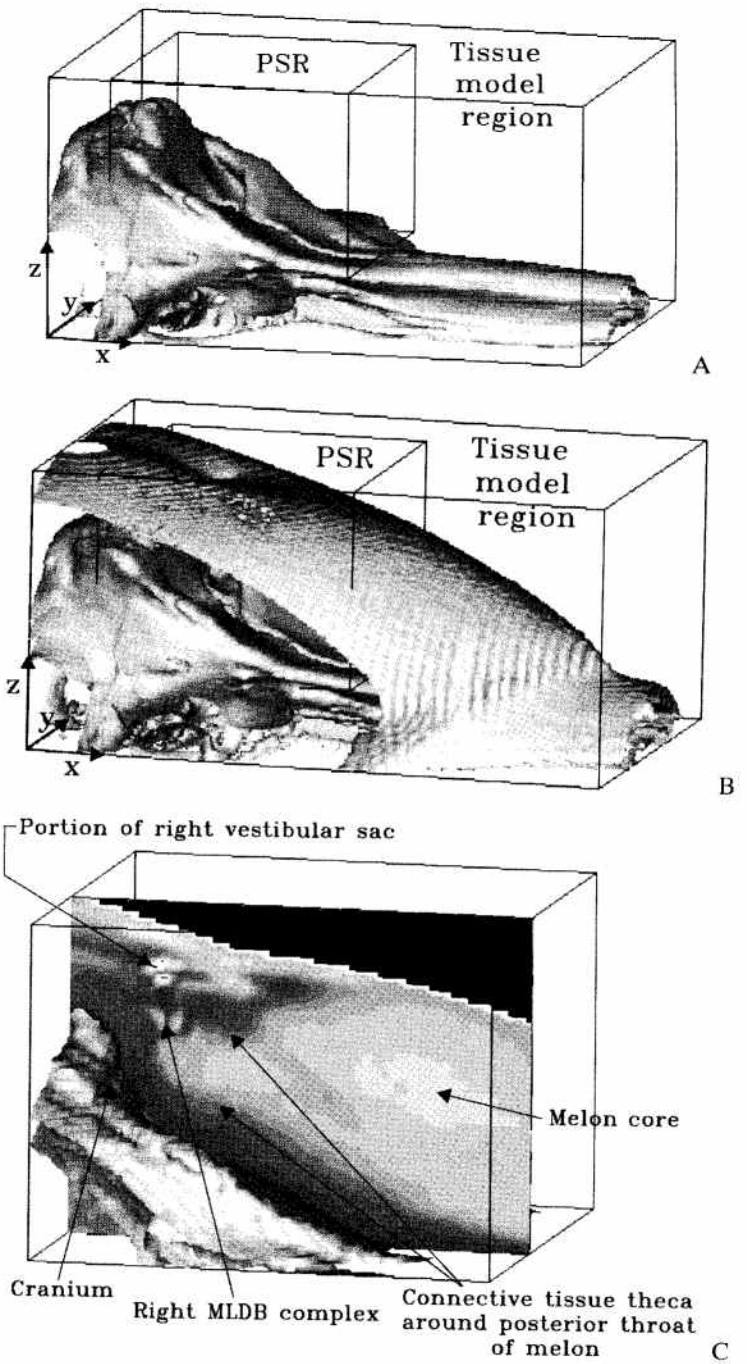

FIGURE 10.5. (A) Visualization of the outer skull isosurface within the region of the CT data set selected for the detailed forehead simulations. (B) Visualization of skin and bone isosurfaces within the same region of the CT data set. The potential acoustic energy density within the subvolume labeled "PSR" was visualized. (C) Perspective view of a parasagittal CT data slice through the center of the right MLDB complex in the PSR region. Several tissue structures are indicated and the skull isosurface added in order to provide positional reference in later diagrams of the results of the inverse simulations.

negative x-axis, which corresponds (via reciprocity) to a forward beam direction of 5° above the positive x-axis. Recall the logic of the inverse procedure: the maxima produced by a return beam will correspond to those positions within the tissue model that could, were sources placed there, best

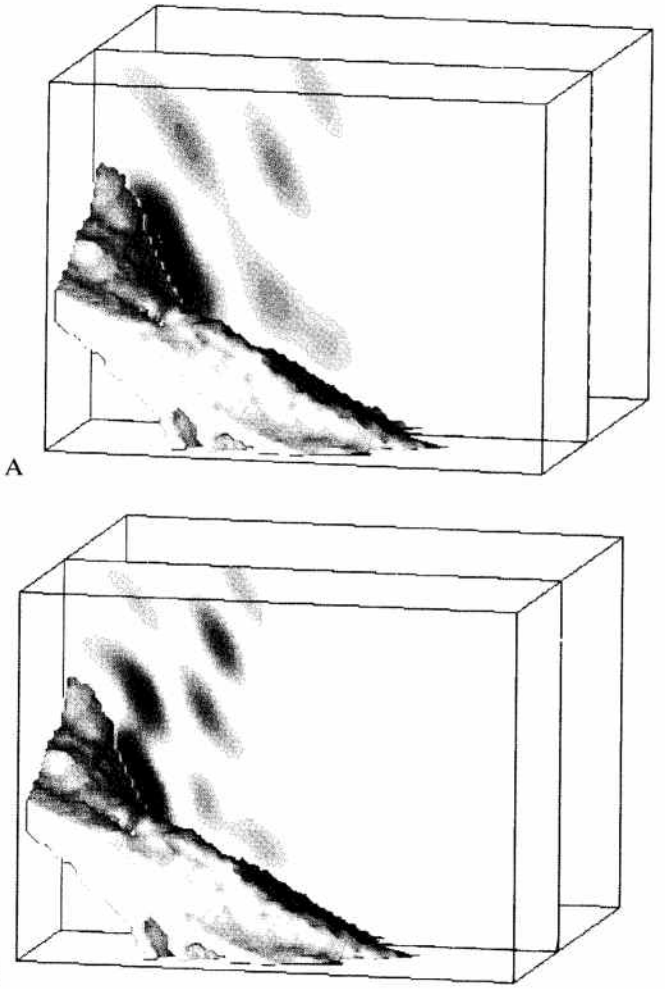

FIGURE 10.6. (A) and (B) Perspective illustrations of the potential energy density in parasagittal slices of the PSR containing the maxima for inverse $(\theta, \phi) = (5°, 0°)$ simulations with the skull-only model at frequencies of 50 kHz and 75 kHz, respectively. (C) and (D) Positions of the "hypocenters" from inverse $(\theta, \phi) = (5°, 0°)$ simulations with the skull-only model at four frequencies. (C) is a PSR view of the maxima positions from the right and (D) is a PSR view from the front. For multiple maxima, the size of the symbols is scaled to the energy of the maxima represented. The skull isosurface was added to all diagrams for positional orientation.

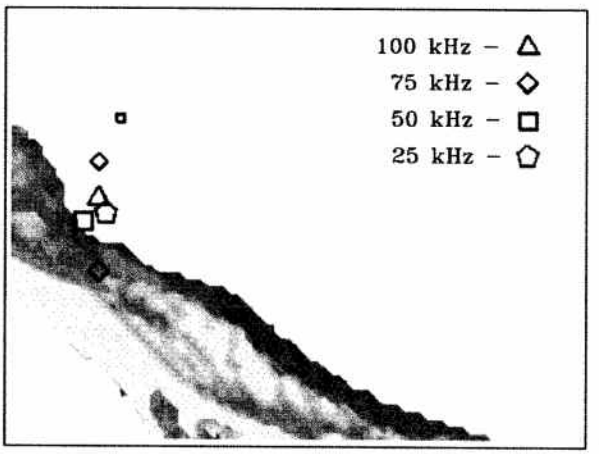

C

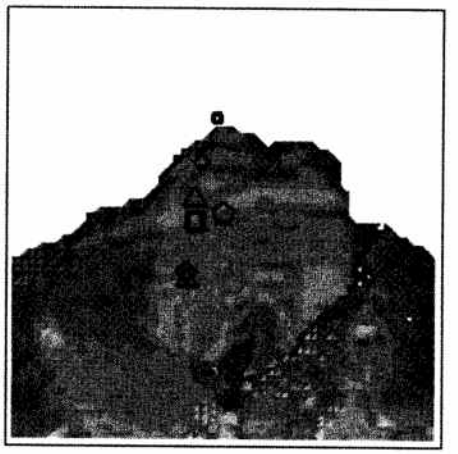

D

FIGURE 10.6. *Continued*

recreate a forward (emission) beam in the direction opposite the return beam. Focal tissue properties should be observable as a clustering of maxima over the relevant angles and frequencies. Because sonar beam angles are not well known for *D. delphis*, a limited range of vertical angles was tested for each tissue model in Aroyan (1996). In Figures 10.6a and b, patterns of spatial interference caused by reflections off of different portions of the skull surface are evident. Note that the positions of the maxima appear below the (right) MLDB and also up against the frontal bone. The maxima lying immediately against the skull may be caused in part by the process of reflection at hard surfaces, where the pressure amplitude nearly doubles, and the potential energy density almost quadruples. Indeed, the reader is cautioned against jumping to the conclusion that any one of these single frequency focal maxima is optimal for the animal—especially for the

simpler tissue models. As we shall see, multiple maxima appear in most of the models, although the ambiguity decreases significantly when the soft tissue density and velocity information and the air sacs are included. This is analogous to the situation in inverse seismologic simulations where ambiguity decreases with the accuracy and completeness of the geologic models assumed.

The positions of these 'hypocenters' for inverse simulations at the four frequencies, 25, 50, 75, and 100 kHz, are shown in two PSR projections (viewed from the right and the front) in Figures 10.6c and d for the same direction of return propagation (an inverse $(\theta, \phi) = (5°, 0°)$ beam in the angular coordinate system of Figure 10.A1a in the Appendix). The maxima up against the skull is shown when it exists and also the "soft tissue" position (not against the skull) of highest potential energy density for each frequency. The general trends in the positioning of these skull-only focal maxima are clear. Along an anterior to posterior axis, foci only occur in the region of the upper narial depression, within a distance of about 3 cm (generally less) from the slope of the frontal bone. Along a transverse axis, they appear to fall along a line running up the right side of the narial depression, and not on the left. The two lowest foci appear to lie within the vertical range of the right nasal plug, while the main cluster lies roughly 1 cm behind and below the location of the right MLDB.

Consider now the emission patterns that result from placing point sources at the focal positions of the skull. Figure 10.7 illustrates the far-field emission distributions computed (using the forward simulation and extrapolation techniques discussed in Section 2.1 and Appendix A) for a point source with a frequency of 75 kHz placed at the $(\theta, \phi) = (5°, 0°)$ inverse simulation point of maximum potential energy density shown in Figures 10.6c and d (see Appendix A for explanation of the mapping of emission directions). Peak emission angles (in degrees) and the directivity indexes for these patterns are included in the figure. While a fair amount of energy is projected to the sides and upward, the skull by itself is capable of forming significant forward beams solely via reflection off of its upper surface for sources placed in the vicinity of the right narial depression. Emission simulations at 25, 50, and 100 kHz also resulted in forward beams similar to Figure 10.7, with directivity indexes increasing approximately linearly with the logarithm of frequency.

3.2 Skull and Soft Tissue Simulations

For the skull and soft tissue model, the density and velocity of all points within the selected forehead region (see Figures 10.5a and b) were assigned by the mappings described in Section 2.2. Because these mappings assign all air CT scan voxels to the background seawater density (1.03 g/cc) and velocity (1,500 m/s) values, air sac regions were effectively "filled" with seawater in this model.

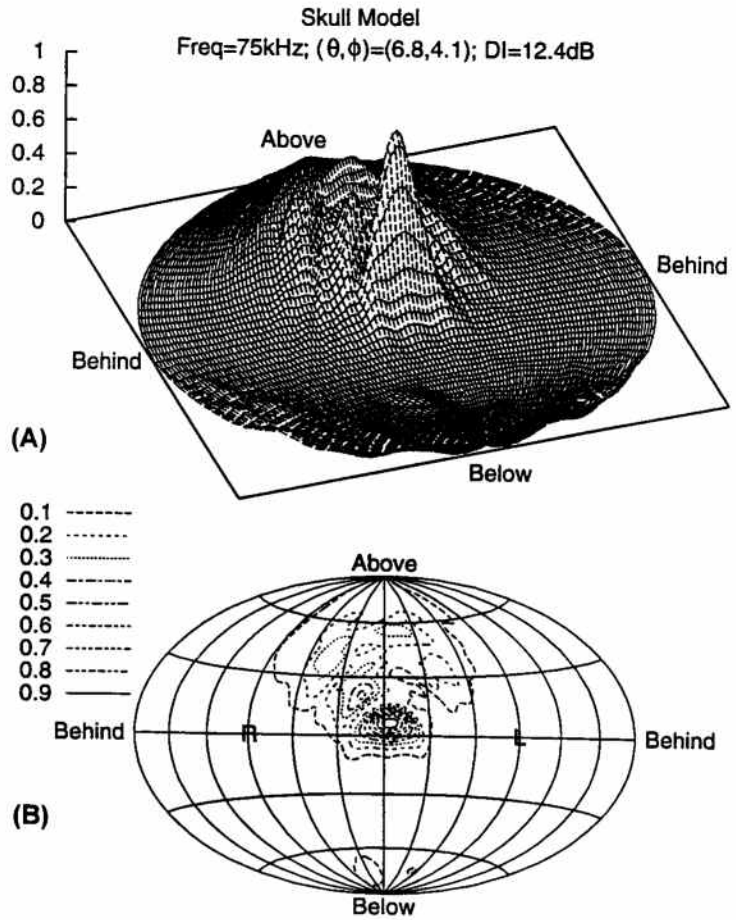

FIGURE 10.7. Extrapolated far-field emission pattern at 75 kHz for the skull-only model. The source point was the focal position of highest potential energy density obtained from a 75-kHz inverse $(\theta, \phi) = (5°, 0°)$ simulation. Diagram (A) plots intensity as height in a perspective view of the global far-field data. Diagram (B) is a contour plot of the same data projected downward into the plane of the global map. Direction angles (in degrees) of the emission peak and the directivity index for this pattern are indicated.

A surprising shift occurs in the patterns of acoustic energy flow through the PSR region when the soft tissues of the dolphin's forehead are added into the model. Figures 10.8a and b illustrate the potential energy density $W_{\text{potential}}$ in the parasaggital PSR slices that contained the soft tissue maxima from inverse $(\theta, \phi) = (5°, 0°)$ simulations with the skull and soft tissue model at frequencies of 50 and 75 kHz. The patterns no longer look simply like spatial interference caused by specular reflection from the hard skull

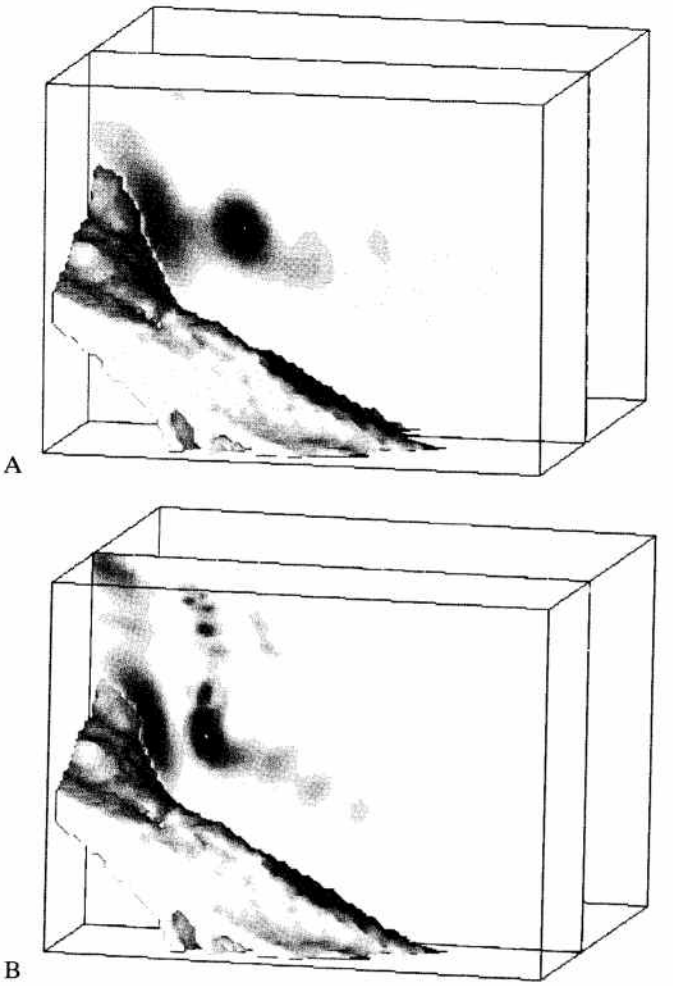

FIGURE 10.8. (A) and (B) Perspective illustrations of the potential energy density in parasagittal slices of the PSR containing the soft tissue maxima for inverse $(\theta, \phi) = (5°, 0°)$ simulations with the skull and soft tissue model at frequencies of 50 kHz and 75 kHz. (C) and (D) Positions of the "hypocenters" from inverse simulations with the skull and soft tissue model at four frequencies. (C) is a PSR view of the maxima positions from the right; (D) is a PSR view from the front. For multiple maxima, the size of the symbols is scaled to the energy of the maxima represented. The skull isosurface was added to all diagrams for positional orientation.

surface. A clear tendency toward collimation or channeling of energy is exhibited by the melon tissues. Energy is channeled in both vertical and horizontal sections back through a region passing approximately 1.0 cm ventral to the right MLDB complex. This channeling is most pronounced

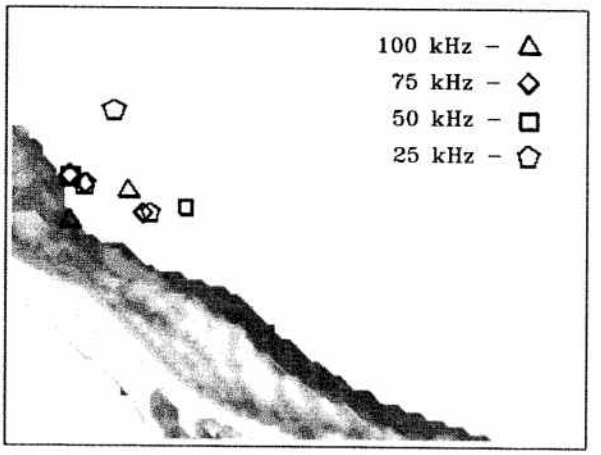

C

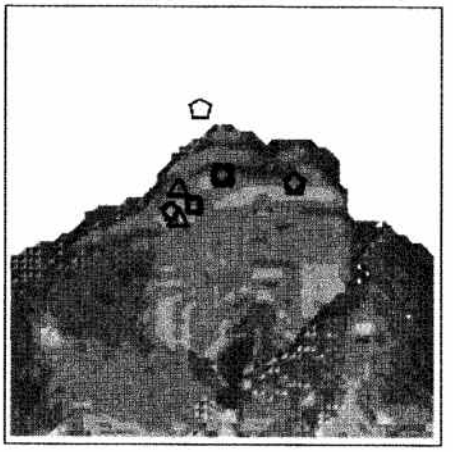

D

FIGURE 10.8. *Continued*

within the posterior throat of the melon. The results at 25 and 100 kHz (not pictured here) exhibit this same behavior.

Figures 10.8c and d shown the locations of the PSR focal maxima (viewed from the right and the front) from simulations at frequencies of 25, 50, 75, and 100 kHz for an inverse $(\theta, \phi) = (5°, 0°)$ beam direction in the skull and soft tissue model. The maxima up against the skull is shown if it exists and the soft tissue position of highest potential energy density for each frequency. Again, note that the focal positions occur in the nasal passage region within a few centimeters of the cranial slope. Most appear on the right side, but two were located within 3 mm of the cranial slope on the left side (left-sided maxima occurred in three instances with this model only). These left-sided maxima were positioned about 1.5 cm posterior

to, and about 1.0 cm medial to, the center of the left MLDB complex. Also, three maxima of the inverse $(\theta, \phi) = (10°, 0°)$ pattern (not pictured here) occurred against the skull down within the right nasal plug. Generally, however, the foci not lying against the skull appeared below the right MLDB.

The far-field emission pattern at 75 kHz for the skull and soft tissue model is illustrated in Figure 10.9. The distribution was computed for a point source at the 75-kHz inverse simulation foci of maximum potential energy density shown in Figures 10.8c and d. Note that addition of the soft tissues has narrowed the skull-only emission pattern. The melon (in combination with other soft tissues of the forehead) collimates much of the energy projected to the side and upward by the skull alone. The increased directivity index indicates a significant contribution by the melon to the formation of narrow biosonar beams.

3.3 Skull, Air Sacs, and Soft Tissue Simulations

The air sac model illustrated in Figure 10.3 was added to the skull and soft tissue model to form the skull, air sacs, and soft tissue model. This combined model constitutes a fairly complete representation of the dolphin's forehead tissues, although the air sac model was conservative (see Section 2.2). The results of this model are therefore of special interest.

Figures 10.10a and b illustrate the 10% isosurface level of the maximum PSR potential energy density $W_{\text{potential}}$ (viewed from above and from the right, respectively) for an inverse $(\theta, \phi) = (5°, 0°)$ skull, air sacs, and soft tissue simulation at 75 kHz. Energy collimation is clearly occurring in the melon, with strong channeling in both the vertical and horizontal directions back through a region passing approximately 0.7 cm ventral to the right MLDB complex. Again, this channeling is most pronounced within the posterior throat of the melon. Note that the anterior melon also appears to be functioning as a lensing element (note the curvature of the anterior energy fronts in Figure 10.10a). Except for slightly sharper maxima, parasagittal PSR slices of the energy density in this model look very similar to the results pictured in Figure 10.8 for the skull and soft tissue model.

The focal maxima locations are plotted in Figures 10.10c and d (as viewed from the right and the front, respectively) for inverse $(\theta, \phi) = (5°, 0°)$ simulations at frequencies of 25, 50, 75, and 100 kHz in the skull, air sacs, and soft tissue model. Again, the maxima up against the skull is shown when it exists and the soft tissue position of highest potential energy density for each frequency. Note that all of the foci occur on the right side of the nasal passages, not on the left, and that they have become fairly well grouped along the guide channel of the posterior melon, which passes roughly 0.7 cm below the right MLDB. Besides the $\theta = 5°$ maxima shown in Figure 10.14, focal positions were also determined for vertical return angles of 15°,

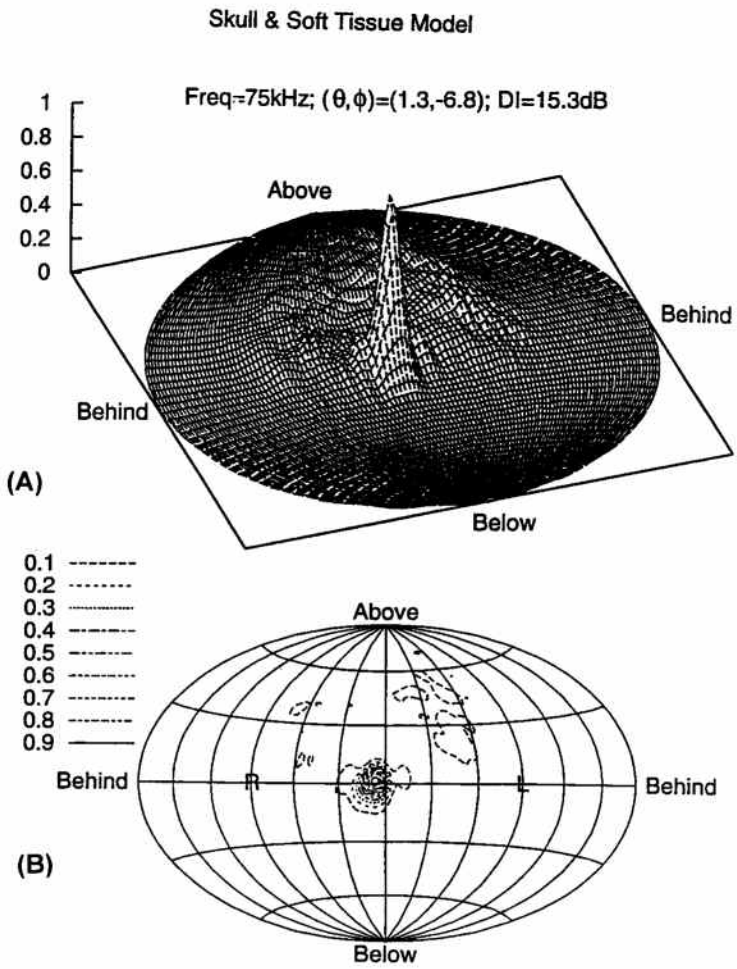

FIGURE 10.9. Extrapolated far-field emission pattern at 75 kHz for the skull and soft tissue model. The source point was the focal position of highest potential energy density obtained from a 75-kHz $(\theta, \phi) = (5°, 0°)$ inverse simulation. Diagram (A) plots intensity as height in a perspective view of the global far-field data. Diagram (B) is a contour plot of the same data projected downward into the plane of the global map. Direction angles (in degrees) of the emission peak and the directivity index for this pattern are indicated.

10°, 0°, −5°, −10°, and −15° in the skull, air sacs, and soft tissue model. The focal positions appear well clustered throughout the $\theta = 5°$ to −5° range of inverse results, and the average position of the cluster does not move appreciably.

Emission patterns, however, are most tightly focused for sources placed at the $\theta = 5°$ inverse maxima of the skull, air sacs, and soft tissue model.

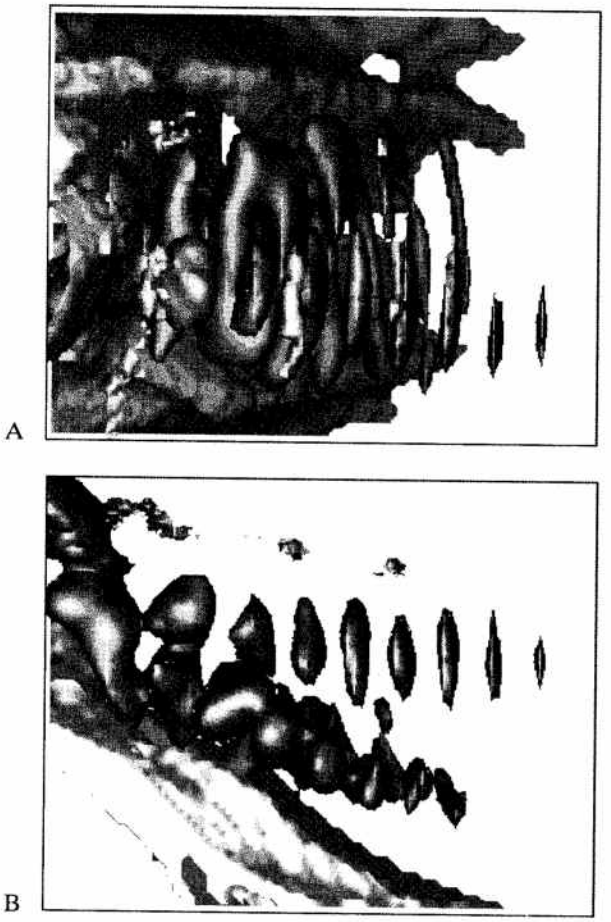

FIGURE 10.10. (A) and (B) Visualizations of the isosurface at 10% of the PSR potential acoustic energy density from a 75-kHz inverse $(\theta, \phi) = (5°, 0°)$ simulation with the skull, soft tissue, and air sacs model. (A) is a view of the PSR from above and (B) is a view of the PSR from the right. (C) and (D) Positions of the "hypocenters" from inverse $(\theta, \phi) = (5°, 0°)$ simulations with the skull, soft tissue, and air sacs model at four frequencies. (C) is a PSR view of the maxima positions from the right and (D) is a PSR view from the front. For multiple maxima, the size of the symbols is scaled to the energy of the maxima represented.

Figures 10.11 and 10.12 plot the far-field emission patterns that resulted from placing 25-, 50-, 75-, and 100-kHz point sources at the focal maxima of the inverse $(\theta, \phi) = (5°, 0°)$ simulations with this model. The complete forehead tissue model does indeed produce well-focused and relatively uniformly directed forward beams. Again, directivity indexes for these patterns increase approximately linearly with the logarithm of frequency. Incomplete diffraction rings are also noticeable at the lower frequencies.

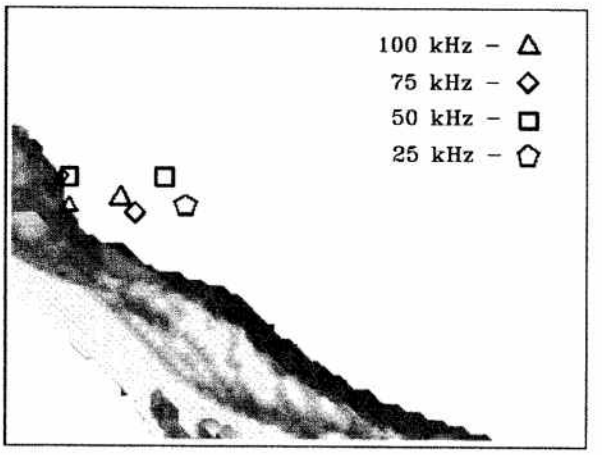

C

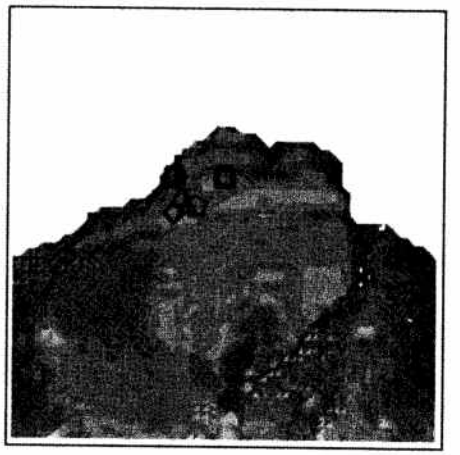

D

FIGURE 10.10. *Continued*

3.4 Moved Source Simulations

Finally, we illustrate emission patterns for the complete skull, air sacs, and soft tissue model when the source point is moved to four locations previously conjectured to be the biosonar signal source location. Patterns were computed for 50- and 75-kHz point sources placed at the tip of the larynx, within the node of the right nasal plug, at the center of the left MLDB complex, and at the center of the right MLDB complex. The full head (half-resolution) model was used in the laryngeal source simulation; the truncated forehead (full-resolution) model was used in the other three moved source simulations.

Figure 10.13 illustrates the 75-kHz far-field pattern contours for these four conjectured source locations. Note that the laryngeal source location

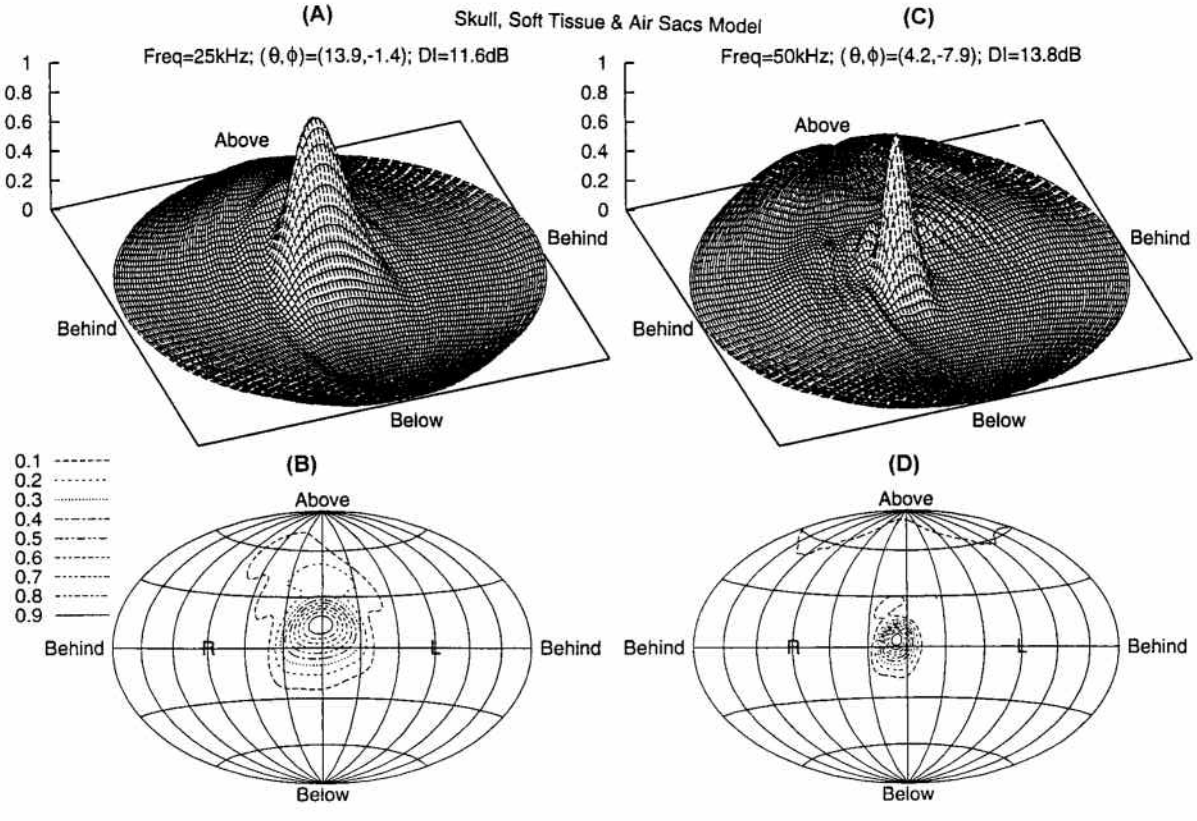

FIGURE 10.11. Extrapolated far-field emission pattern at 25 and 50 kHz for the skull, soft tissue, and air sacs model. The source points were the focal positions of highest potential energy density obtained from inverse $(\theta, \phi) = (5°, 0°)$ simulations.

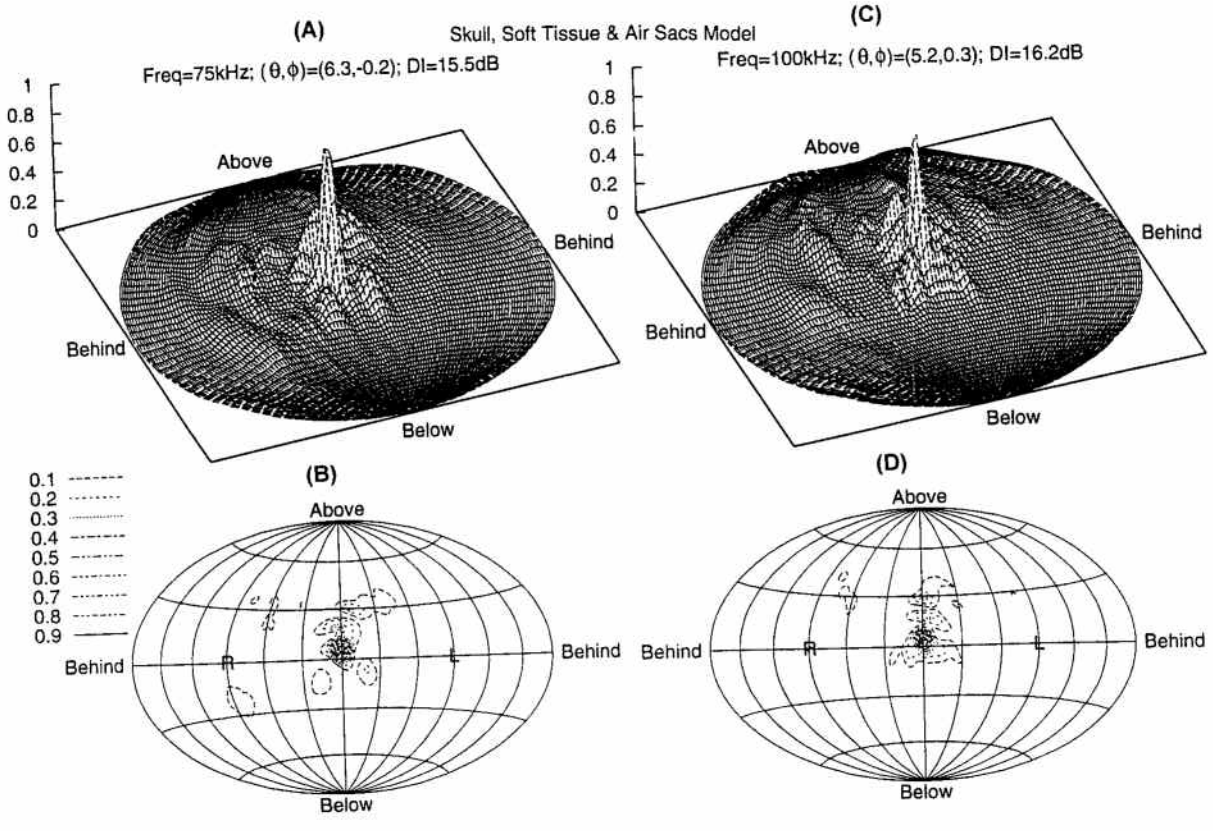

FIGURE 10.12. Extrapolated far-field emission pattern at 75 and 100 kHz for the skull, soft tissue, and air sacs model. The source points were the focal positions of highest potential energy density obtained from inverse $(\theta, \phi) = (5°, 0°)$ simulations.

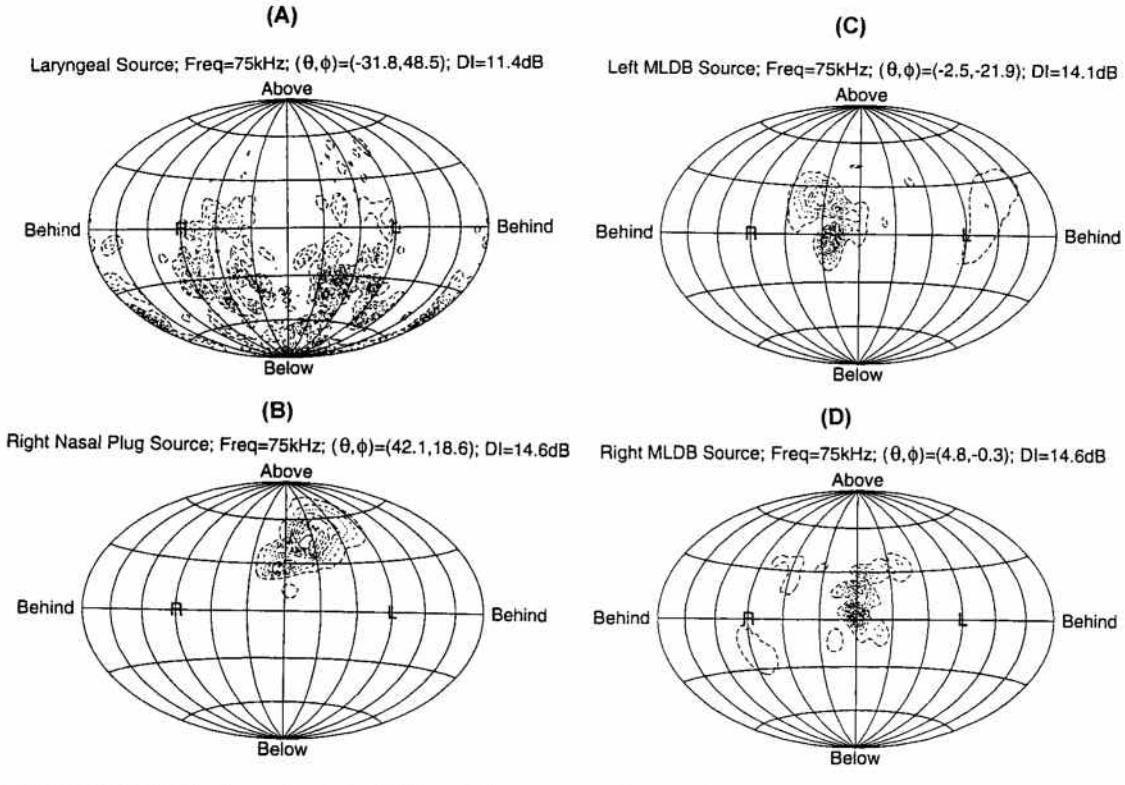

FIGURE 10.13. Contour plots of extrapolated far-field emission patterns for a 75-kHz point source placed at various tissue locations. (A) Placed at the tip of the larynx in the full head model. (B) Placed within the right nasal plug node in the complete forehead model. (C) Placed at the center of the left MLDB complex in the complete forehead model. (D) Placed at the center of the right MLDB complex in the complete forehead model.

mainly produces scattered downward and sideways emissions. Sources placed in the right nasal plug node projected sound forward at rather high vertical angles (average $\theta = 38°$) and somewhat left of forward. The left MLDB source location projected beams averaging about 26° right of forward. The right MLDB source location produced approximately centered beams with some secondary lobe energy into higher vertical angles.

4. Discussion of Results

As with all bioacoustic tissue simulations, the results of this study are dependent on both the accuracy of the wave propagation techniques and on the fidelity of the tissue models to in vivo tissue geometry and acoustic properties. Although shear wave modes were ignored, the accuracy of the compressional wave propagation techniques was demonstrated in Aroyan (1996) to be excellent. Tissue geometry is generally well represented in high-resolution X-ray CT data, but some displacement of the supranarial soft tissues may have occurred through air sac collapse. However, the scan methodology of Cranford (1992) was developed to minimize gross postmortum tissue distortion. While approximate, the technique used to model the acoustic properties of soft tissues is based on established tissue mass density scan practices and on the measured acoustic properties of mammalian and unique delphinid tissues. In addition, simulation results were found to be quite robust with respect to biologically reasonable variation of the HU-to-density and HU-to-velocity model mappings. This may in part be due to the relatively short tissue propagation paths (generally less then 10 wavelengths) involved in the simulated emission processes. While many opportunities exist to refine the analysis, the work presented here is sufficient to reach a number of interesting conclusions.

The role of the skull in acoustic beam formation has been investigated using both acoustic sources and ray tracing techniques (Evans et al. 1964), using lightbulb-as-source techniques (Dubrovskiy and Zaslavskiy 1975), using acoustic sources with and without soft tissue present (Romanenko 1973), and using two-dimensional bioacoustic simulations (Aroyan 1990; Aroyan et al. 1992). The results of the three-dimensional skull-only forehead simulations have corroborated and extended the conclusions of these previous studies. The common dolphin's skull plays a predominant role in beam formation by establishing the basic focal geometry of the forehead. The skull by itself is capable of forming significant forward beams solely by reflection off of its upper surfaces. Focal maxima were found only in the immediate vicinity of the asymmetrically enlarged right narial depression, and not elsewhere. The fact that these maxima occurred only on the right side of this depression and not on the left suggests that the focal geometry of the skull is functionally related to its asymmetry. Because air sacs cover portions of the skull surface in the vicinity of the nasal passages, the focal

geometry demonstrated here apparently also shapes and supports the highly reflective flesh-air sac boundaries. In the common dolphin, skull acoustic asymmetry parallels the asymmetry of the refractive soft tissues of the forehead, as discussed below.

Much speculation has surrounded the acoustic role of the fatty melon tissues of the delphinid forehead. Wood (1964) suggested that the melon may both focus and acoustically couple internally generated sound to seawater. Sound speed measurements on the melon of a Pacific bottlenose dolphin (Norris and Harvey 1974) revealed a low-velocity core and a graded outer shell of high-velocity tissue. A number of biomolecular studies have confirmed that the lipids of the delphinid melon are chemically distinct from other body fats and blubber. Evans et al. (1964) found that the presence of the soft tissue of the bottlenose dolphin's forehead caused narrower beams to be emitted than were produced by the skull alone. Romanenko (1974) measured horizontal beam widths with the whole head that were roughly half as wide as the widths obtained using the skull alone for frequencies of 80 kHz and higher. Previous two dimensional simulations (Aroyan 1990; Aroyan et al. 1992) suggested that a melon velocity profile of the magnitude measured by Norris and Harvey (1974) is capable of mild focusing.

The current project substantiates the results of these earlier investigations of the acoustic function of the delphinid melon. The 3D skull and soft tissue simulations have demonstrated that the melon and other soft tissues of the *D. delphis* forehead significantly narrow the main forward beam, corroborating the results of Evans et al. (1964) and Romanenko (1974), and confirming the conjectures of Wood (1964) and Norris (1968). The melon's efficiency in narrowing the horizontal beam width generally appears greater than its effect on the vertical width. In addition, the inverse skull and soft tissue simulations demonstrated a pronounced tendency towards collimation or channeling of acoustic energy within the posterior throat of the melon. The posterior throat of the melon appears effective as a partial wave-guide, while the larger forward lobe of the melon has been confirmed to operate as a lens in the acoustic emission process.* Perhaps the magnitude of these effects explains the extraordinary metabolic investment that the specialized melon tissues represent in the evolution of odontocete cetaceans, as suggested by Morris (1986).

---

* See the discussion of fundamental acoustic mechanisms in Aroyan (1996, pp. 28–34). A three-component model of the delphinid biosonar emission system is proposed consisting of an impulsive source mechanism (the MLDB source hypothesis of Cranford et al. 1987), a damped resonant chamber surrounding this source (formed by the partially air-bounded soft tissue of the delphinid nasal passages), and a projector of the ensuing signal consisting of the skull, the melon and other soft tissues of the forehead. Simplified calculations with this model correctly predict the frequency ranges and modal/bimodal signal structures of several odontocetes as a function of signal source level and body size. The surprising consequences of this simple model will be discussed in later reports.

To illustrate the physical basis of melon focal behavior, Aroyan (1996) plotted the density, velocity, and impedance structure in a two-dimensional slice through the *D. delphis* melon and forehead using the modeling techniques of Section 2.2. These plots reveal an impedance matched melon-seawater interface, confirming the matched impedance hypothesis of Wood (1964). They also reveal a broad velocity depression in the anterior melon that narrows posteriorly to form a well defined channel through the rear throat of the melon. The broad velocity depression is indicative of a lensatic function for the anterior melon, as conjectured by Wood (1964) and proposed in greater detail by Norris (1968). The posterior velocity channel appears analogous to a flared wave-guide. The velocity of the melon "wall" rises somewhat gradually to a maximum of about 20% above the velocity of the channel in the posterior melon. While a velocity reduction of 20% within a waveguide of uniform geometry may permit highly efficient guiding of specific wavefunctions, the short and widely flared throat of the posterior melon in this dolphin is probably best characterized as a partial or "leaky" wave-guide of biosonar clicks.

An incomplete model of the nasal air sacs has been shown to improve the forward reflection of energy projected upward, sideways, and downward by the skull and soft tissue model. Addition of the air sacs into the model always raised the directivity indexes of the patterns, although the importance of this contribution varied with frequency. Generally speaking, the air sac model was effective in forward collimation of energy projected upward, sideways, and downward by the skull along, while the melon was effective in narrowing (focusing) the main forward lobe. Both the air sac model and the melon, however, contributed to both effects. Nevertheless, a precise evaluation of the relative contribution of the nasal air sac system to beam formation must await better information on the exact configuration of the air sacs during click production.

The biosonar signal source tissues in the common dolphin were found to be localized within a remarkably small volume of the nasal passages. A dramatic clustering of inverse simulation foci for all frequencies tested in the complete model implicates approximately 1 cc of tissue centered about 0.7 cm below the center of the right MLDB complex as the most plausible "hypocenter" of the dolphin's biosonar clicks. However, the posterior lip of the MLDB complex is often displaced dorsally with respect to the anterior lip in postmortem specimens (Cranford et al. 1996). It is possible that some or all of the soft tissues of the supranarial region were displaced slightly from their air-metering configuration during biosonar click production. In the author's opinion, the clustering of focal points best supports the conjecture that the *right* MLDB complex is the source tissue of the pulsed biosonar signals of this dolphin. Inverse simulation foci were notably absent from other previously proposed source locations including the left MLDB, the larynx, and the right nasal plug node. In the complete model, foci were found only on the right side of the nasal passageway and not on the left. The nonviability of the larynx and right nasal plug as source locations for

biosonar clicks was further illustrated by forward extrapolations of the far-field patterns produced by point sources placed at the tip of the larynx and within the node of the right nasal plug in the complete model.

A surprising degree of acoustic asymmetry was also discovered. In the *D. delphis* specimen, forehead asymmetry is developed to a point where very different beams are produced by left and right MLDB sources. The centers of the left and right MLDB complexes are separated by about 3.4 cm in this specimen. Sources placed just below the right MLDB complex produced well-focused forward-directed beams, while sources placed at the left MLDB produced somewhat scattered emission patterns peaked roughly 26° to the right of center forward. These differences have a significant bearing on the conjecture that both complexes may be used simultaneously to produce coherently interfering beams (Cranford et al. 1996). Dual MLDB source simulations above 50 kHz (not illustrated here) have shown that coherent forward beaming is constrained by the well separated pattern peaks. Even if dual MLDB source coordination on a time scale of microseconds were biologically possible, phasing would have little effect on the resulting multi-lobed emissions.

Perhaps the central conclusion of the current investigation was that the forehead tissues of the *D. delphis* model exhibit a simple focal structure for forward-directed beams, with the right MLDB (or slightly below) as focal center. While the behavioral evidence generally does not support the occurrence of multi-lobed emission patterns in delphinids (Dormer 1979; Mackay and Liaw 1981; Au 1993), it is possible that previous experiments have not been designed to encourage this behavior. Some dolphins appear capable of selectively producing sonar pulses at either the left or right MLDB (Cranford, Chapter 3). Nevertheless, it remains probable that the asymmetrically enlarged tissues of the right side are indeed specialized for click production (Mead 1975). As suggested by Heyning (1989), "there may have been selection for a single sound generating source in the narial region in order to avoid interference generated from two sound sources." The development of separate motor control would also have contributed to the avoidance of sonar beaming problems.

The overall beam forming capability of the forehead tissues demonstrated here for the common dolphin is impressive. We have seen that the complete forehead tissue model produces relatively uniformly directed and well focused forward beams when appropriate source locations are used. The −3 dB beam widths of approximately 12° (vertical) and 11° (horizontal) in the 100 kHz pattern are consistent with the experimentally measured broadband (peaked near 120 kHz) beam widths of 10.2° (vertical) and 9.7° (horizontal) for *Tursiops truncatus* (Au et al. 1978). The directivity indexes computed here for the complete *D. delphis* model, however, fall roughly 10 dB below those reported for *T. truncatus* (Au et al. 1978; Au 1980). Taking both frequency and size differences into account for these animals, a disparity of roughly 5 dB remains. In this context, it is important to note that

two peculiarities of the model may have contributed to lowering the computed directivity indexes. First, the incomplete air sac model may have lowered the computed indexes at all frequencies. Second, because point sources emit uniformly in all directions, one expects the use of point sources in these simulations to have lowered the computed directivity indexes by amounts that depend on the frequency and assumed geometry of the signal generator. For these reasons, the demonstrated focal characteristics of the forehead tissues are expected to be conservative.

The forehead tissue structures of the common dolphin are representative of members of the odontocete family Delphinidae having an intermediate-to-moderate value of soft tissue asymmetry (Cranford 1992). It is expected that similar if not identical mechanisms operate in all delphinids exhibiting intermediate-to-moderate soft tissue asymmetry (including *T. truncatus*). It is also reasonable to suggest that similar mechanisms may operate in all odontocetes that possess forehead tissue morphologies resembling those of the common dolphin.

The techniques utilized here to investigate the biosonar system of *D. delphis* are applicable to many other marine mammal species. Investigation of odontocete species with better studied biosonar emission fields (i.e., *T. truncatus, Delphinapterus leucus, Pseudorca crasidens*) would serve to test the generality of the emission mechanisms discussed above. In addition to sound emission, the same techniques may be used to model hearing. Aroyan (1996) simulated individual right and left ear receptivity patterns and tissue reception pathways in the common dolphin using techniques that are widely applicable to other marine mammals. Extensions of the method for modeling the acoustical parameters of biological tissues from X-ray CT data presented in Section 2.2 may enable a host of bioacoustic applications. Finally, the power of combined propagation and extrapolation techniques has yet to be exploited in several areas of physical acoustics.

5. On the Physics of Sound Production in the Blue Whale

Blue whales (*B. musculus*) produce loud low-frequency underwater sounds, providing a practical tool to study whale distribution and movements (Thompson and Friedl 1982; McDonald et al. 1995; Stafford 1995). The blue whale is not only the largest animal alive, but is also the loudest, making it an excellent choice for sound production mechanism study. Previous publications on the physics of the baleen whale sound production mechanism have concentrated on bubble resonance (Harris 1964; Barham 1973), a phenomena where a given air volume at a given depth will resonate to produce sound efficiently at an acoustic frequency that can be calculated. We propose that a Helmholtz resonance better fits the observations in that, unlike bubble resonance, Helmholtz resonance provides efficient

constant frequency sound production over changing depths, allowing the whale improved efficiency in monotonic sound production. Previous studies have provided anatomical information and speculation on how baleen whales may produce sound (Hosokawa 1950; Yablokov et al. 1972; Sukhovskaya and Yablokov 1979; Purves and Pilleri 1983; Quayle 1991; Reidenberg and Laitman 1992, 1993; Haldiman and Tarpley 1993). Our goal is to integrate the physics of sound production with blue whale laryngeal anatomy to develop a verifiable model of how the blue whale produces sound.

Before applying physical constraints to sound production in blue whales, it is helpful to understand the variability within the blue whale call repertoire. Calls from the blue whales observed off the California shore have been the most studies, and can be divided into four fundamental types, shown in Figure 10. 14: (A) typically the first call of a series, consisting of about 20 pulses spaced about 0.8 s apart, with each pulse subdivided into multiple, time-offset nonharmonic components; (B) a harmonic sound typically 19 s in duration, sweeping or stepping down slightly in frequency from about 20 Hz to 16 Hz; (C) a 9- to 12-Hz upswept tone preceding a type B call; (D) an 80- to 30-Hz downsweep typically 2 to 5 s in duration, often produced by multiple animals as counter-calls and not produced in combination with the other call types. It is only the type B calls that provide a unique constraint on the sound production model. Only the type B call is of continuous long duration such that the sound production mechanism is unlikely to be able to recirculate the air used in producing the call. The calls shown in Figure 10.14a were recorded in the Santa Barbara Channel using sonobuoy arrays for localizing the sound source in combination with visual localization, leaving little doubt that blue whales were the source of these sounds. Similar calls have been recorded from blue whales off California, Oregon, and Baja California, Mexico (Thompson et al. 1992; D'Spain et al. 1995; McDonald et al. 1995; Stafford 1995; Rivers 1997). Type B calls have reported source levels up to 190 dB re 1 μPa in recordings made off San Nicolas Island, California (Aburto et al. 1997). The duration of the type B calls illustrated in Figure 10.14 ranges from 16 to 21 s. The type A and B blue whale calls often occur in patterns with regular pauses between calls and longer pauses during breathing periods (Cummings and Thompson 1971; McDonald et al. 1995; Stafford 1995).

Blue whales have geographic call character variation, the animals off the west coast of North America having similar call character for more than thirty years (Thompson 1965) while blue whale calls from other regions are distinctly different (Weston and Black 1965; Kibblewhite et al. 1967; Cummings and Thompson 1971; Northrup et al. 1971; Thompson and Friedl 1982; Alling and Payne 1988; Alling et al. 1991) suggesting learned call character within geographic variations as occurs in birdsong (Kroodsma 1996). The type B call off the west coast of North America provides the longest continuous sound from blue whales known to the authors.

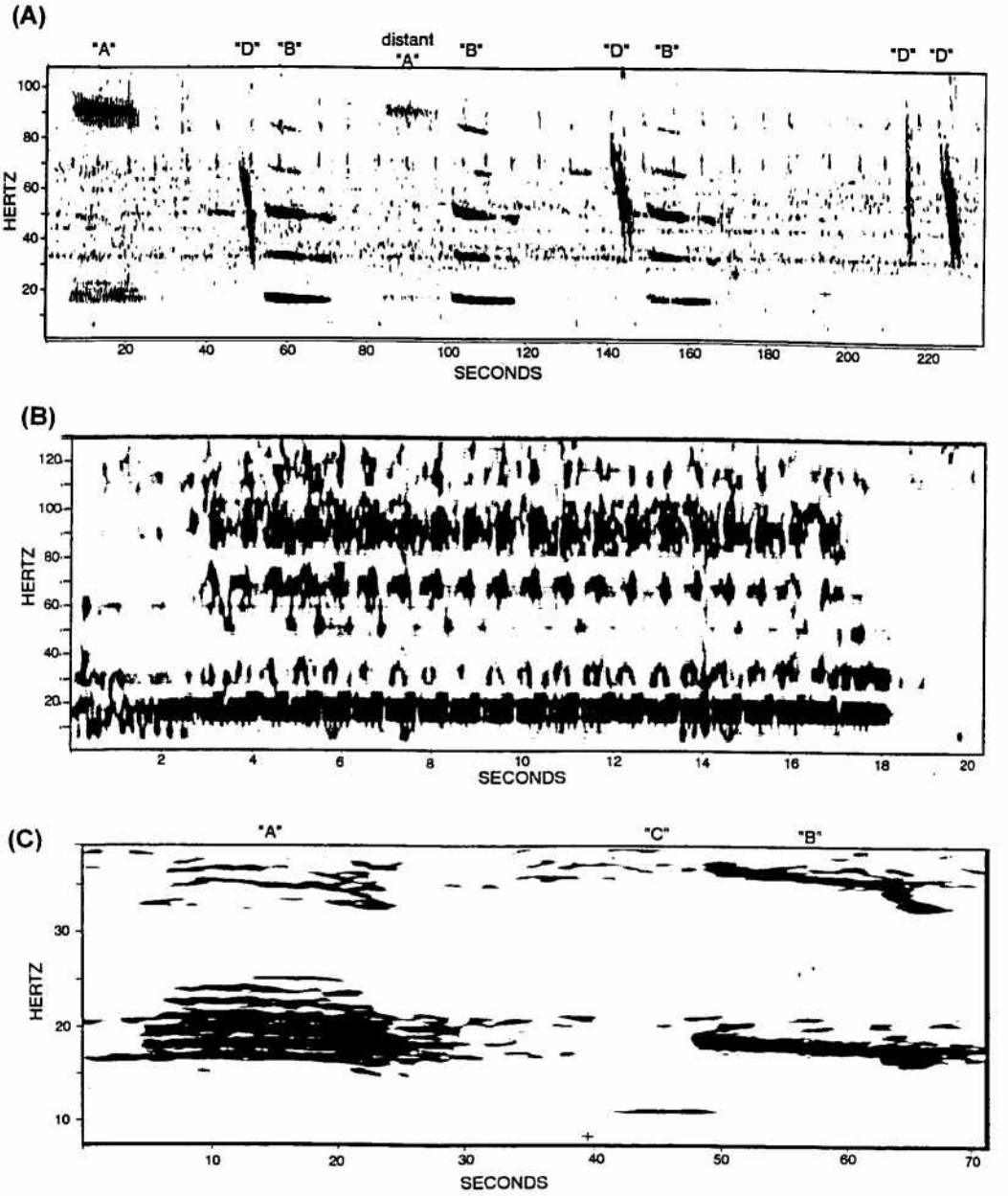

FIGURE 10.14. Examples of the four most common blue whale call types (A–D) recorded off the west coast of North America are shown as spectrograms. (A) Sequence of type "A" and "B" calls recorded on a sonobuoy array in the Santa Barbara channel, California, the loudest "A"–"B" series is believed to be produced by a single animal, interspersed with some short downsweep "D" calls produced by a second animal. Weaker calls can be seen in the background from another animal. The spectrogram was computed with 1 s FFT length, 97% overlap, and a Hanning window. Frequency response is boosted 1.5 dB/octave above 10 Hz. *See text for details on parts B and C.*

6. Blue Whale Sound Production Model

6.1 *Water, Solid, or Air*

All possible mechanisms for sound production in the blue whale must involve radiating sound into seawater, but the oscillating media could, theoretically, be made of water, bone, or air within the whale. Sound can be produced underwater by fluctuations in water pressure (water), as in a hydrodynamic oscillator (Albers 1965, pp. 176–177); by vibration of rigid materials (solid), as in the sounds produced by snapping shrimp (Albers 1965, pp. 221–227) and possibly the jaws of whales (Brodie 1993); or by oscillations of an air-filled chamber (air), as is the case in most biological sound production systems. A water-filled source may be possible in a whale using a hydrodynamic oscillator based on the large water-filled pleated ventral cavity of a blue whale, perhaps using the flexible walls as a waveguide to shorten the dimensions required to achieve resonance at 17 Hz (Fletcher 1992). Such a water-based sound source would appear to be very inefficient due to losses associated with moving the whale's ventral tissues. Another possibility is to design a resonant 17-Hz oscillator based on shear mode vibrations of the lower jaw bone of a blue whale, but again this would be an inefficient sound radiator, the bone dimensions being significantly less than the 22-m optimum length for an efficient dipole radiator. Systems able to compress water or bone are considered less efficient than air-filled systems and require much higher differential pressures. The system that is the least complex, most versatile, and most efficient is an air-filled cavity oscillation.

6.2 *Volume Displacement Requirements*

Just as a human singer can hold a note only until all the air in the lungs is expired, we believe the blue whale can only produce a continuous call of given intensity and frequency for some maximum duration dependent on the volume of air available. We assume the whale has no system equivalent to a series of pumps and valves that would allow continuous recirculation of air. The volume of air required to produce an underwater sound is then dependent on the displacement required to produce each cycle of a sound of given intensity, given frequency, and the resonance of the system, which is a direct measure of the efficiency of producing that displacement. The resonance quality factor is proportional to the efficiency and is discussed later, but first we calculate the displacement requirements.

The intensity of an underwater sound produced by oscillation of an air-filled cavity can be directly related to the associated volume displacement required to produce each cycle of that sound. The whale is compact in an acoustical sense, so that the displacement is the total net fluctuation in the volume of the whale each cycle, requiring air to be alternately compressed and released. Assuming this compression occurs as air is moved past a fluc-

tuating valve, so that there is no resonance or recirculation of the air, the minimum volume of air required for producing the sound can be computed for a given duration, loudness, and frequency. The fundamental equations relating displacement to sound intensity for the case when the wavelength is long relative to the dimensions of the source are derived in numerous texts as variations of the following form (Harris 1964, p. 239; Seto 1971, p. 85; Lighthill 1978, p. 19):

$$P_0 = \frac{\rho\omega^2 V}{4\pi r} \tag{5}$$

where: P_0 is the sound pressure level in N/m^2 or Pa (i.e., 185 dB re 1 μPa = 20 log $(I/10^{-6})$ = 1,770 N/m^2), ω is $2\pi f$ where f is frequency, ρ is the density of seawater = 1,025 kg/m^3, V is the volume change required to produce the required pressure per cycle of the sound, and r is the distance from the point source at which the pressure is measured or 1 m for our reference standard. Rearranging terms and substituting for ω gives:

$$V = \frac{P_0}{\rho\pi f^2} \tag{6}$$

The total air flow volume required for a monotone of given duration can be calculated versus frequency and intensity using Eq. 6 and assuming no resonance. The harmonic type "B" call intensities of 190 dB RMS re 1 μPa are measured over a bandwidth including both fundamental and higher harmonic frequencies (Aburto et al. 1997) while the air volume requirements are primarily from production of the fundamental frequency (also called the first harmonic), thus we must determine the intensity of that portion of the call. Most of the energy in a blue whale "B" call is in the first and third harmonics. The energy distribution between the fundamental and third harmonic is variable, but the third harmonic is typically less intense. If we assume the energy is equally divided between the first and the higher harmonics, then the first harmonic intensity is 3 dB less than the total. The estimated first harmonic intensity is then 187 dB re 1 μPa at 1 m. Figure 10.15 is a plot of Eq. 6 illustrating the sensitivity of the volume calculation to frequency and intensity of the call. The shaded box in Figure 10.15 is plotted for frequency and intensity best estimates of the type "B" blue whale call first harmonics recorded offshore of California, indicating that the flow volume requirement is 800 to a 1,100 liters assuming no resonance. Future call recording studies may show a tradeoff between intensity, frequency and duration, with the volume requirement remaining nearly fixed.

6.3 A System for Underwater Sound Production

The production of sound requires a source of energy and a vibrating element (Zemlin 1988). Our previous discussion concludes air is likely the medium being oscillated and it is a logical extension to assume that the

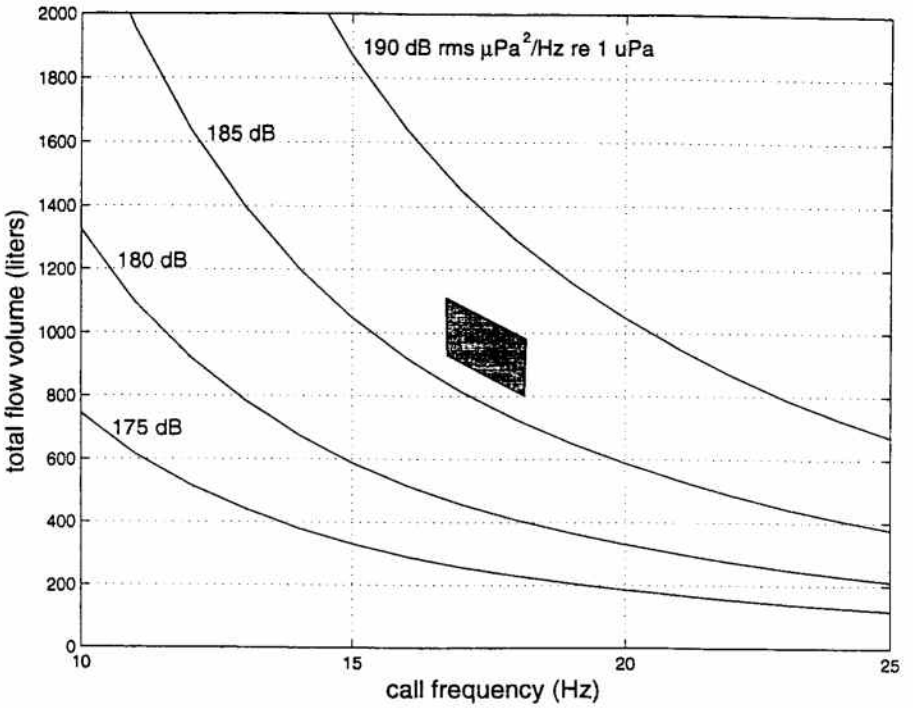

FIGURE 10.15. A plot of Eq. 6 illustrating the sensitivity of the volume calculation to frequency and intensity of the call. The shaded box is plotted for frequency and intensity best estimates of the type "B" blue whale call first harmonics recorded offshore in California, indicating that the flow volume requirement is 800 to 1,100 liters assuming no resonance.

whales' lungs must be involved to provide the great volume of air required by blue whale type "B" calls. The simplest source model for generating sound is a pulsating sphere, where the radius varies sinusoidally with time, this being called a monopole source. If the wavelength of the sound produced is sufficiently long relative to the size of the source, the shape of the expanding and contracting volume need not be spherical to meet the required assumptions. The more complicated dipole source consists of either two monopole sources placed some distance apart and being of opposite phase, one expanding while the other is contracting, or of a vibrating element such as a beam. Figures 10.16a and b illustrate the two most basic types of air-filled oscillators, monopole and dipole. The wavelength of the 17-Hz sound, produced by a blue whale, is about 90 m in seawater. A mature blue whale offshore of California averages 21 m long overall (Gilpatrick et al. 1995), but its air-filled cavities are only several meters in length. Whale dimensions that are small relative to an acoustic wavelength preclude all but a simple acoustic source (monopole) since more complex sources need to be near or greater than one-quarter wavelength long to operate effi-

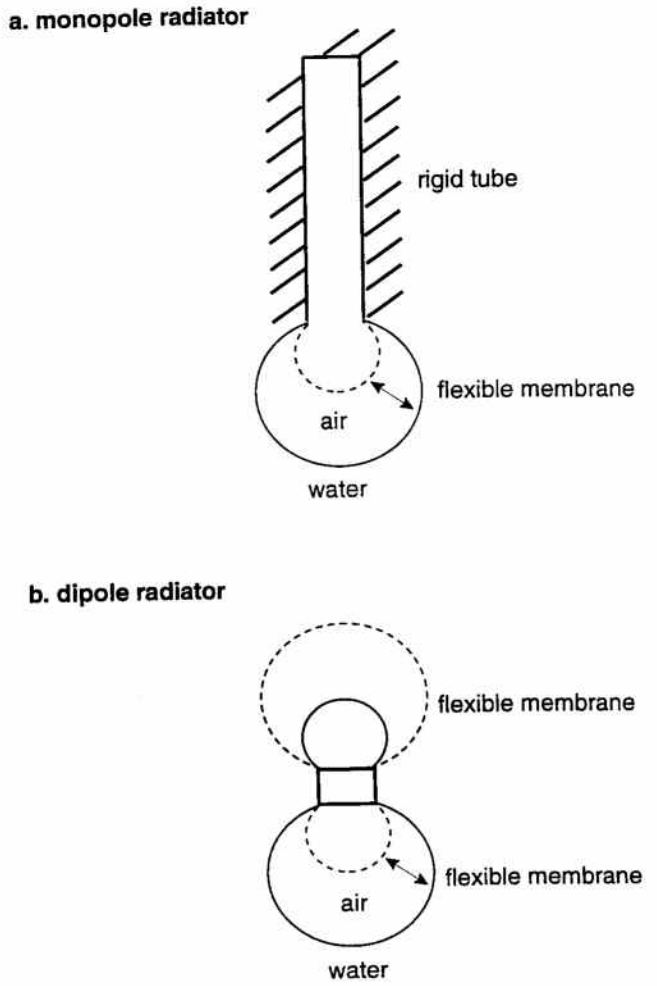

FIGURE 10.16. The two most basic types of air-filled oscillators, monopole and dipole.

ciently. Considering the case of a dipole source filled with air, the possible anatomical separation between the two poles in a blue whale could be only about 1 m instead of the 22.5 m that would be ideal for sound production. While a dipole source can produce sound with a separation only 1/22 of the ideal, it will operate very inefficiently, requiring huge volumes of air to be shifted between the two halves of the dipole (Figure 10.16b). This makes the monopole source the most likely sound production mechanism for the blue whale.

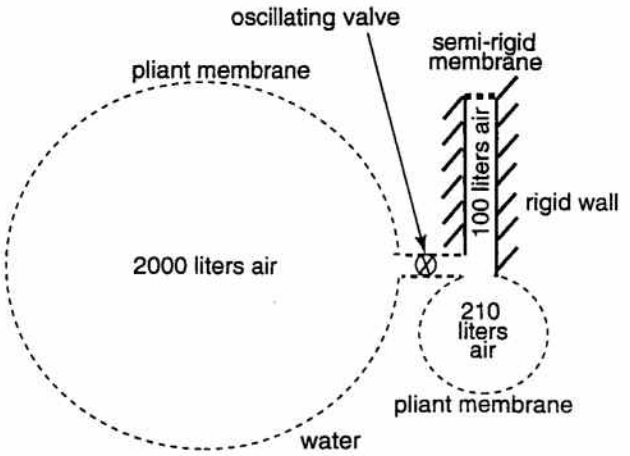

FIGURE 10.17. A simple system containing all the elements of our sound source model. Features from the blue whale anatomy have been included in the drawing.

We propose that the monopole source will ideally include a rigid element to avoid becoming a dipole source in the case of the whale. For example, moving air back and forth between two balloons underwater, at frequencies where the wavelength is much longer than the separation between the balloons, results in an inefficient dipole source. A rigid component in the system allows the air to compress without a corresponding expansion, allowing the oscillating radiator to act as a monopole source. Without a rigid component the whale would need to use simultaneous muscular contraction and expansion over the entire air volume.

A simple system containing all the elements of our sound source model is illustrated in Figure 10.17, where we have included features from the blue whale anatomy in drawing the figure. For instance, the rigid component is appropriately sized to represent the nasal passages, the pliant components to represent the lung and the laryngeal sac. It would be possible to leave out the laryngeal sac portion of this system, but then the sound radiator would have to be either the semirigid boundary corresponding to the nasal plugs or the lungs. We leave the details of the oscillating valve, the equivalent of the vocal cords in human speech, until the discussion on anatomy. The system shown in Figure 10.17 will provide the volume displacements needed to produce a blue whale type "B" sound as it is raised or lowered through the water column, the pliant membrane compressing or expanding, moving air into or out of the rigid chamber corresponding to the nasal passages. The primary energy source for this sound production system is the change in pressure produced by diving or ascending. Most of the energy required to operate this sound production system is used to store the air

rather than to produce the sound. It becomes obvious the whale's lungs cannot provide the nearly 10 bar of pressure differential needed to provide such a volume displacement while remaining near the surface. The whale would be required to provide a slight differential pressure through muscular compression of its lungs in order to keep the laryngeal sac inflated preferentially during a dive and the whale would need to provide muscle control over the oscillating valve. It seems possible the type "B" call is only produced during ascent, thus eliminating the need for the whale to provide positive differential pressure with its lungs as would be needed during descent. If air were to escape from the system during sound production, such losses would limit a whale's total call production between breathing periods, making the observed call series impossible. It is generally believed that no air escapes from baleen whales during sound production (Conner 1994, p. 80), although whalers do report occasional "blow wakes," believed to correspond to air expulsions, from submerged *B. musculus* while being pursued with active sonar (Haines 1974).

The larger pliant membrane in Figure 10.17 will be completely collapsed at a depth where the total air volume under pressure is just sufficient to fill the smaller pliant and rigid volumes:

$$Z_c = \frac{P_0 V_L}{\rho g V_n} \tag{7}$$

where Z_c is the dive depth in m, P is the water pressure, and P_0 is pressure at the surface, V_L is the surface lung volume, ρ is the water density = 1,025 kg/m^3, g is the acceleration due to gravity = 9.8 m/s^2, and V_n is the volume of the combined nasal passages and laryngeal sac.

As the system in Figure 10.22 is submerged, the volume flow rate of air that passes the oscillating valve can be calculated as follows with m_n defined as

$$m_n = V_n \rho_n \tag{8}$$

as the mass of air on the narial side (including laryngeal sac) of the oscillating valve corresponding to the arytenoid cartilages, V_n is the volume of air on the narial side, and ρ_n is the air density on the narial side. There must be a fluctuating pressure in the laryngeal sac and nasal passages, but for the purpose of calculating the change in the density of the air due to changes in depth we assume the pressure on the narial side of the valve, is on average, equal to the hydrostatic pressure in the seawater. The volume of the air decreases with increasing pressure as the air is compressed during descent. The density of air in the lungs increases linearly with depth as does the pressure in the lung, P_L:

$$\frac{P_0}{\rho_0} = \frac{P_L}{\rho(z)} \tag{9}$$

where P_0 is pressure at the sea surface, ρ_0 is air density at the sea surface, and $r(z)$ is air density at depth z. If the volume V_n is constant, then air must flow from the lungs through the valve during descent, or back into the lungs during ascent from the narial side. If it is constant, the rate of change of the mass of the air on the narial side is proportional to the rate of change of the density:

$$\frac{\partial m_n}{\partial t} = V_n \frac{\partial \rho_n}{\partial t} \tag{10}$$

The mass flow rate through the valve, $\dot{m}$, can be related to the volume flow rate, Q, by the air density in the lung, ρ_L:

$$\dot{m} = Q\rho_L \tag{11}$$

The volume flow rate can be expressed:

$$Q = \frac{V_n}{P_L}\frac{\partial \rho_n}{\partial t} \tag{12}$$

From Eq. 5, the change in air density with time is proportional to the change in pressure:

$$\frac{\partial \rho}{\partial t} = \frac{\rho}{P}\frac{\partial P}{\partial t} \tag{13}$$

Combining Eqs. 12 and 13, the volume flow rate, Q, is

$$Q = \frac{V_n}{P_L}\frac{\partial P_L}{\partial t} \tag{14}$$

The volume displacement, V_D, across the arytenoids from the lung side to the narial side is the integral of the volume flow from surface to collapse depth:

$$V_D = \int_{t_1}^{t_2} Q dt = V_n \ln\left[\frac{P(t_2)}{P(t_1)}\right] = V_n \ln\left[\frac{V(t_2)}{V(t_1)}\right] \tag{15}$$

When substituting the maximum values the volume displacement $V_{D\max}$ becomes:

$$V_{D\max} = V_n \ln\left[\frac{V_n}{V_n + V_l}\right] \tag{16}$$

Equation 12 describes the volume of air moving past the oscillating element during a dive from the surface to the lung collapse depth. The total displacement of the whale decreases with the dive as the air is compressed. Sound is produced if the valve interrupts the flow of air so that air is alternately dynamically compressed and released in the nasal passages so that the total displacement of the whale fluctuates at the frequency of sound production. The solution to Eq. 16 allows a comparison between a whale's

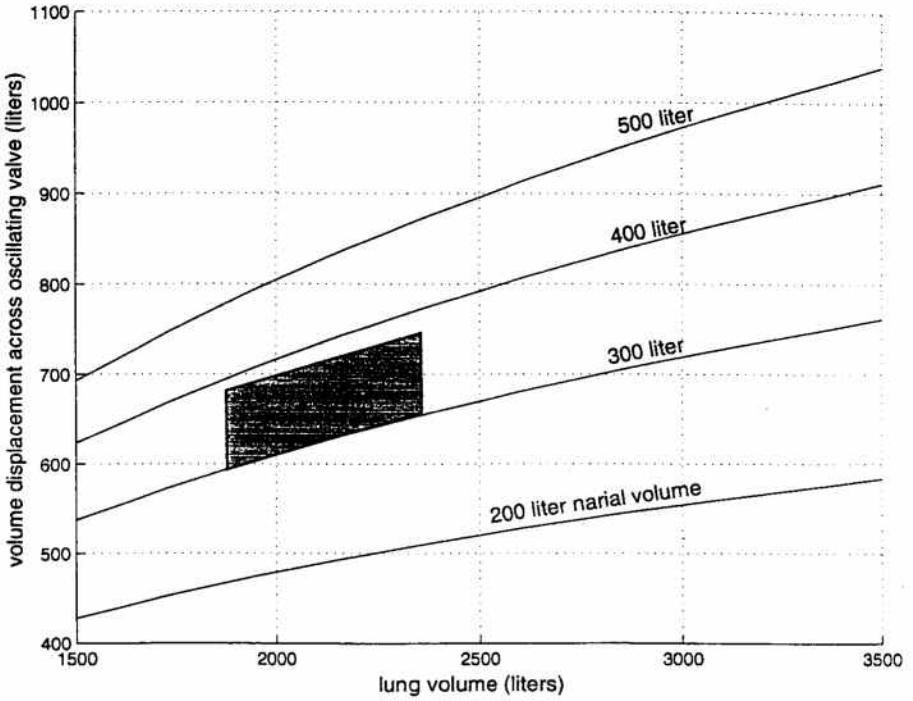

FIGURE 10.18. Total volume flow (sound production capacity) for a range of values for both lung volume and the volume on the rostral side of the arytenoids, which includes the laryngeal sac and nasal passages. The shaded box represents the range of best anatomical estimates for a typical offshore California blue whale.

sound production capacity based on anatomical estimates, and the volume requirement estimates for blue whale calls (Figure 10.22). Figure 10.18 graphs total volume flow (sound production capacity) for a range of values for both the lung volume and the volume on the rostral side of the arytenoids, which includes the laryngeal sac and nasal passages. The shaded box in Figure 10.18 represents the range of best anatomical estimates for a typical offshore California blue whale, as discussed later. These estimates suggest that the whale can move a maximum of 600 to 750 l of air past the oscillating element. These flow volume estimates are less than the air flow volume requirements of Figure 10.15, which limit the duration and loudness of a type "B" call assuming no resonance. In order to achieve a 19-s duration 17-Hz monotone of 187 dB re 1 μPa, the flow volume would need to be about 1,100 l instead of 650 l. From this we conclude that either our anatomical volumes are too small, our call intensity is erroneously high, or resonance has improved the efficiency of the system, a topic further discussed later.

7. Supporting Evidence

7.1 Anatomical Air Volumes

The volume of the lungs and associated air chambers in blue whales provide a check on the plausibility of the proposed sound production model. Large whales' lung volumes have been reviewed previously (Lockyer 1981). Adult blue whales found off California are typically about 21 m long (Gilpatrick et al. 1995), and would have a lung capacity of about 2,000 l. This estimate is based on extrapolation from other mammals and agrees well with estimates based on nozzle-type flow volume calculations using blow rise times and nasal passage dimensions combined with percentage estimates of expiration volume. A significant error may still exist in this lung capacity estimate as methods based on thoracic cavity volume are substantially larger. Following the analysis of Lockyer (1981), we have largely discounted the thoracic cavity volume estimates.

The capacities of the blue whale laryngeal sac and nasal passages are somewhat less studied, requiring extrapolation from a combination of related anatomical measurements. The descriptions of blue whale laryngeal anatomy available to the authors (Turner 1870; Beauregard and Boulart 1882) are somewhat confusing due to the use of archaic Latin names. The description of Beauregard and Boulart (1882) describes two animals, one as a 12-m female *B. musculus* and another as a 3.6-m male fetus of *B. sibbaldi*, though both Latin names are considered to describe blue whales today (Tomilin 1957; True 1983), despite significant differences in the appearance of the thyroid cartilage in these two animals. The description of Turner (1870) is based primarily on a 5.9-m male fetus taken from an animal that measured 24 m on the curve of the back. References are also made to an earlier description (Malm 1867) that was not available. The larger of the two blue whale larynxes described by Beauregard and Boulart (1882) had an incompletely preserved laryngeal sac, thus only the fetus provided a complete laryngeal sac length. We prefer to infer likely dimensions of the blue whale laryngeal sac primarily from a 17.75-m female fin whale, *B. physalus*, (Purves and Pilleri 1983) having dimensions proportionally consistent with the smaller intact blue whale specimens described. From these descriptions we infer a 21-m blue whale would have a laryngeal sac length of 1.35 m, depth of 0.45 m, and width of 0.35 m for a volume of 210 l before possible pressure expansion.

Although skull measurements for blue whales are relatively well described (Omura, Ichihara, and Kasuya 1970), the dimensions of the nasal passages through the skull are not included, and we have not found nasal passage volumes described for any of the mysticetes. In order to estimate the volume of the nasal passages, a blue whale skull, Los Angeles County Museum # 72562, for which a photograph is published (Heyning 1995, p. 78 foreground) was measured and checked against skull photographs (Yochem and Leatherwood 1985). Uncertainty remains in the thickness of

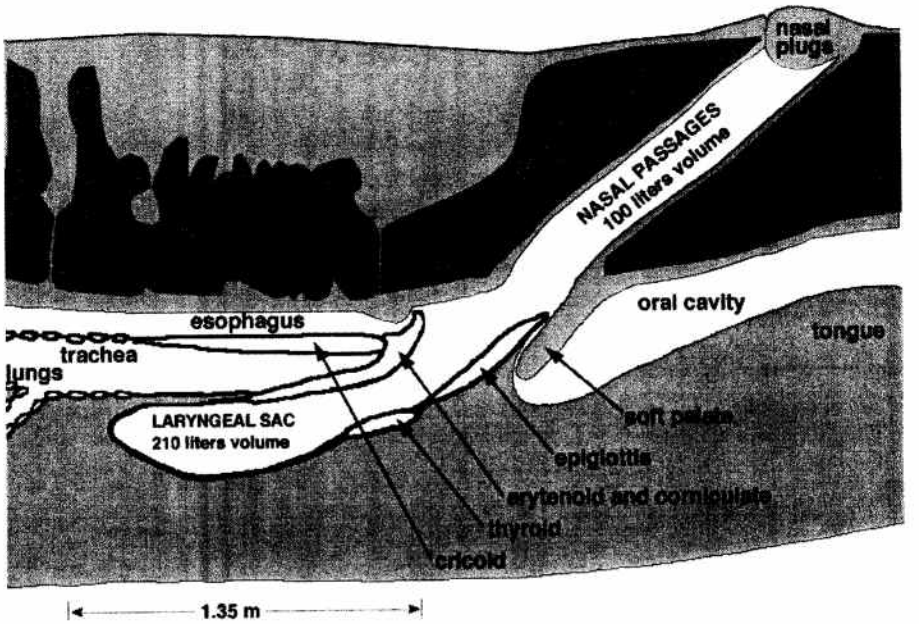

FIGURE 10.19. A sagittal cross section of blue whale laryngeal anatomy drawn to scale for an adult of the size typically found offshore of California. The paired arytenoid cartilages are dashed because they lie outside of the sagittal plane. The three mechanisms that could provide an oscillating valve are the arytenoid cartilages, the U-fold, and the laryngeal sac filling the tracheal lumen as indicated by the curved arrow.

nasal passage linings and the extent to which nasal plugs and the palatal sphincter extend within the nasal passages, but we estimate an air volume length of 1.0 m after scaling to our 21-m long model whale. We estimate the average air-filled diameter of each nasal passage to be 0.25 m for a total nasal passage volume of 100 l (50 l in each). The position and proportions of the air chambers within a blue whale are illustrated in Figure 10.19, drawn with interpretation from anatomical observations on other species of baleen whales (Benham 1901; Hosokawa 1950; Yablokov 1972; Sukhovskaya and Yablokov 1979; Purves and Pilleri 1983; Quayle 1991; Haldiman and Tarpley 1993) where the blue whale descriptions (Beauregard and Boulart 1882) are inadequate. During sound production the epiglottis and arytenoids would be plugged into the nasal passages.

7.2 Oscillating Valve Mechanisms

The two most commonly suggested mechanisms for the oscillating valve are the arytenoid cartilage and the U-fold (Reidenberg and Laitman 1996), although it appears laryngeal sac expansion closing off the tracheal lumen may provide a third possible valve. Figure 10.19 locates these three possible

oscillating valves in an anatomical cross section. The U-fold has been the preferred oscillatory valve for some researchers (Haldiman and Tarpley 1993; Reidenberg and Laitman 1993), while the arytenoid cartilages have been the preferred oscillatory valve mechanism for others (Sukhovskaya and Yablokov 1979; Purves and Pilleri 1983). The presence of well-developed laryngeal folds in the blue whale is described by Beauregard and Boulart (1882), as well as the ability of the paired arytenoid cartilage to close the opening between trachea and laryngeal sac. It may be possible to better determine the roles of the arytenoids and the vocal folds if we can further validate a sound production model. One relevant aspect to consider might be whether the oscillator is reversible. Can the oscillator produce a similar sound from an airflow in either direction? We assume the whale provides muscle control over the oscillating valve, determining the call character.

7.3 Resonators

The calculation of accurate pipe, Helmholtz, or bubble resonance frequencies in the blue whale is beyond the scope of our anatomical knowledge and generally beyond the scope of this discussion even if we were to make the needed biological assumptions. This topic continues to be the subject of considerable importance and interest however, thus we offer some observations. Given the range in the fundamental frequency of the blue whale, both geographic and within a single call, a resonator would have to be of relatively low Q (resonance quality factor) to be sufficiently broad to aid the animal in sound production. Resonance quality factor (Q) is proportional to the energy expended per cycle to the energy stored in the system. High Q systems reduce the amount of air required because the volume of the resonant cavity varies each cycle by more than the volume admitted through the valve. While it has been suggested that low Q bubble resonators would still be useful (Barham 1973), we find a bubble resonator much less applicable than a Helmholtz resonator because it appears difficult to maintain a significant bubble resonance over the depth range required by our model. There are many formulas for bubble resonance, all of which may be correct under different assumptions used to simplify the complexity of the problem in the biological system, but these formulas do not suggest that a significant resonance could be maintained over a significant portion of the depth range from surface to collapse at 90 m, thus limiting the calling whale to a relatively narrow depth range. A Helmholtz resonator consists of an enclosed volume vented through a pipe. On an anatomical basis we suggest the laryngeal sac and nasal passage volume seems a more likely resonator than the total air volume (Barham 1973) given the separation of the two systems at the arytenoids and the relative stability of resonance frequencies within the laryngeal-nasal volume. If the laryngeal sac and nasal passages act as a resonator, then a fluctuating stream of air through the

valve will excite large pressure fluctuations in the nasal passages, which are accompanied by fluctuations in the volume of the laryngeal sac that are large compared to the fluctuations in the air flow through the valve. The sound intensity produced will be larger by the ratio of the volume of the air stream fluctuations to the laryngeal sac–nasal passage volume fluctuations. A realistic resonance calculation for the laryngeal-nasal volume will take account of the Helmholtz resonator formed by the laryngeal sac at the end of the rigid nasal passage and should take account of the semirigid terminations at the nasal plugs. Following the analysis of Fletcher (1992, pp. 178–186) and assuming the anatomical dimensions discussed previously, the sound speed of a 17-Hz wave in a nasal passage tube would have a velocity about 0.65 times that of the sound speed in air. When we combine this lowered velocity with the Helmholtz frequency calculation, applicable because of the short tube length relative to the wavelength, we calculate the resonance frequency as follows (Fletcher 1992, p. 185):

$$\omega_H = c'\sqrt{\frac{S}{lV}} \tag{17}$$

where the angular Helmholtz frequency $\omega_H = 2\pi f$, the propagation speed in the pipe $c' = 0.65$ (330 m/s), the tube cross section $S = \pi r^2 = \pi(0.125\,\text{m})^2$, the length of the tube $l = 1.0$ m, and volume of the laryngeal sac $V = 0.2\,\text{m}^3$. Solving Eq. 17 for the resonance frequency yields 17 Hz before consideration of the semirigid nasal plug terminations on the nasal passages and consideration of the nonrigid nature of the laryngeal sac. We consider it fortuitous that the value from our simplistic calculation is so close to the actual fundamental frequency for our model animal, but it does suggest that some resonance is likely, though it may not be as simple as our calculation suggests.

The resonance quality factor (Q) in biological systems may be as high as 30 (Fletcher 1992), while mechanical systems may have Q values of hundreds or thousands. One approach to estimating the maximum Q for a blue whale type "B" call is by examining the rise time of the fundamental frequency. A resonant system will approach the maximum amplitude in about Q cycles given constant forcing, thus the call rise time, measured in cycles, provides an estimate of the maximum Q for the blue whale. The onset of blue whale call recordings is often altered by constructive or destructive interference from reflections, but examination of numerous calls, each filtered around the fundamental frequency to eliminate harmonics, reveals an overall similarity. A representative "B" call onset is shown in Figure 10.20, where theoretical rise time curves of the form

$$1 - e^{\frac{-\pi f t}{Q}} \tag{18}$$

are plotted for Q values of 6, 10, and 14, appropriate to the transient response of a resonant oscillator driven by a tone burst at the resonant fre-

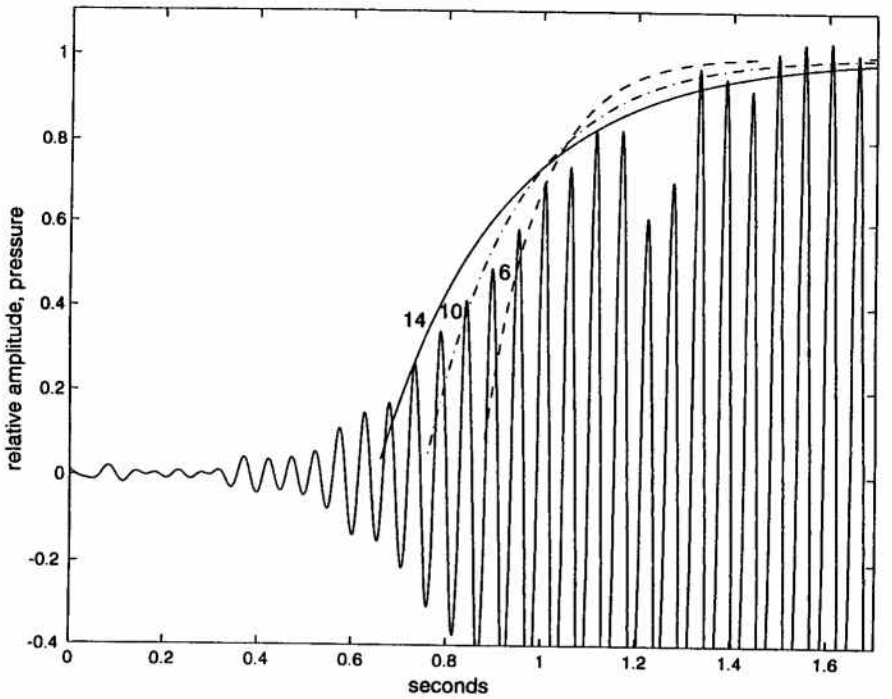

FIGURE 10.20. The start of a waveform of a representative blue whale type "B" call is plotted after passband filtering around the fundamental frequency of 17 Hz. The rate of rise in amplitude provides a maximum estimate of the resonance quality factor (Q) in the system producing the sound. Q values of 6, 10, and 14 are plotted suggesting a best fit of about 10. The actual amplitude rise does not conform well to the theoretical, suggesting the forcing function is not constant and the actual Q of the system is probably much less than 10.

quency (Kinsler et al. 1982). The maximum Q of 10 estimated from Figure 10.20 corresponds to a significant 20-dB amplitude increase due to resonance although the actual Q of the blue whale resonator is probably less. The poor fit of the theoretical curves suggests the forcing function is not constant, thus the actual Q is lower. A 20-dB resonance gain, if actually achieved in a blue whale Helmholtz resonator, would allow production of sounds louder and longer than have been observed, based on the volume estimates of the proposed model, but would require the ability to tune the resonator if the whale is to choose a learned fundamental frequency. Future work is expected to reduce the uncertainties in both the lung volume and call intensity estimates, allowing the equations to solve for Q, the only remaining variable. With our current best estimates for volumes and intensities we need to include a resonance of about 6 dB equivalent to a Q of 2.

Using human speech as an analogy, one might hope to find evidence of resonance in the call character of blue whale calls and relate such charac-

ter to dimensions within the sound production tract. Much of human speech analysis is based on the presence of formants or resonant frequencies in the sounds we make. The character of human speech provides indirect me surements of the speaker's vocal tract, as "each human voice attains its unique tone quality (either speaking or singing) from the particular resonant frequencies of the three *resonant cavities*, the larynx, the mouth and the nasal cavity" (Berg and Stork 1995, p. 108). Blue whale calls appear to lack such formants, thus much of human voice analysis methodology (i.e., homologous deconvolution) may be inappropriate for analysis of blue whale calls. Formants in a blue whale call would be seen as energy corresponding in time and duration with the fundamental frequency, but at nonharmonic frequencies. The type "A" pulsive call character is composed of temporally offset sounds of noninteger frequencies repeated about 20 times in the California animals (Figure 10.14b), thus resonance may play a role in the production of this sound, but because there is an apparent time offset between pulses it is unclear how such a resonant system would work. The type "B" call shows only harmonics, such as would appear in any system driven near its physical limits, and lacks frequencies of noninteger multiples.

8. Predictions from the Blue Whale Sound Production Model

8.1 Dive Profile and Feeding Incompatibility

If the proposed blue whale sound production model is valid, feeding activity would appear incompatible with the repetitive call behavior commonly observed for tens of hours showing only breathing gaps. This incompatibility is predicted both by the necessary connection of the trachea with the palatal sphincter during call production, which may block the esophagus, and by the incompatibility of the required dive profile with searching for and consuming prey. The type "B" call sound production model predicts the whale to be either diving or ascending during call production and limits the maximum type "B" call production depth to the lung collapse depth of 90 m. Matched field acoustic methods (Baggeroer et al. 1993) allow the depth of a blue whale during call production to be measured. Preliminary results from analysis of a single call (D'Spain et al. 1995) suggest the call depth during a type "B" call is 34 m averaged over the entire call duration, a depth consistent with the model, where the depth averaged in time occurs in the upper half of the required 90-m dive or ascent. Further applications of matched field methods to blue whale recordings, and the development of array Doppler and localization methods for motion detection in calling blue whales, may result in significant call depth and vertical motion data that can be used to test the model in the near future.

The intensity of the blue whale type "B" call is nearly constant over the duration of the call, suggesting the ideal dive profile for the sound produc-

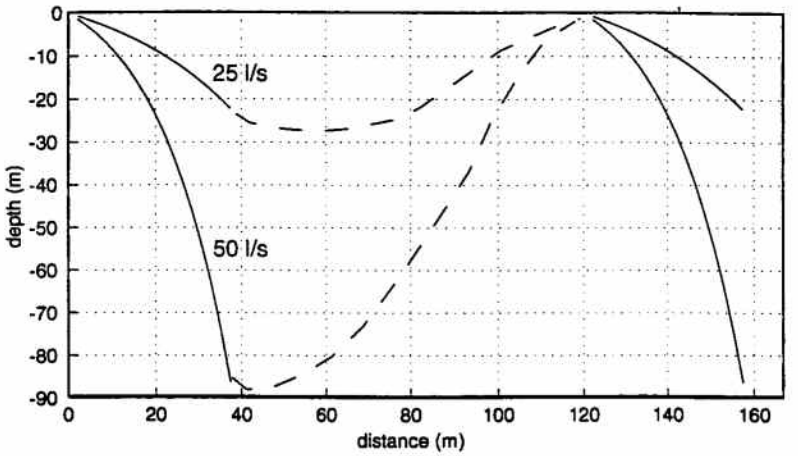

FIGURE 10.21. Constant flow rate dive profiles would not require holding significant differential pressures during sound production, thus balancing the required flow rate across the oscillating valve during diving. Two such dive profiles are plotted, 50 l/s to lung collapse depth with a spacing typical of minimum call intervals (30 s) and a horizontal spacing to match typical speeds (8 km/hr) during call production. The 25 l/s flow rate assumes the whale produces a call 6 dB less intense than it is capable of and does not approach lung collapse depth. The dive profile from left to right corresponds to calling during descent while right to left corresponds to calling during ascent.

tion model would maintain a constant flow rate across the oscillating valve, eliminating significant differential pressures. Using a typical horizontal swim speed (2.2 m/s), Figure 10.21 shows an ideal swim profile for a traveling blue whale producing a series of type "B" calls. In Figure 10.21 we assume the call is only produced while swimming downward, but it is possible the call could be produced in either or both directions. The most typical blue whale call series consists of a 19-s duration "A" call followed about 25 s later by a 19-s duration "B" call, with a less intense 10-Hz call preceding the "B." As shown in Figure 10.19a, however, the whale sometimes repeats the "B" call after an initial "A" call, an important fact since only the "B" call is constrained by the sound production model. Depending on the importance of resonance, which reduces the volume change required to produce a call sequence like that shown in Figure 10.14a, the model predicts the whale must change depth from somewhere near surface to somewhere near lung collapse depth or vice versa for each "B" call produced. Figure 10.21 shows that the sound production model does not require an unreasonable dive profile, if we assume a flow rate of 50 l/s, corresponding to a small resonance in the system (Q = 2) to reduce the total flow needed (by a factor of two?). The average flow rate and the total depth excursion required to produce the sound is markedly reduced if the Q of

the resonance is higher. We also show profile for a flow rate of 25 l/s corresponding to a Q of 4. The shallower dive profile corresponding to a Q of 4 would indicate the whale called at an intensity less than it is capable of because it did not use all the air in its lungs, assuming we have the anatomical volumes correct. The variation in the depth of the blue whale during calling is the major testable hypothesis of the proposed model.

8.2 A Dive Depth Limit?

A question related more to blue whale anatomy than to sound production is. Can the blue whale avoid flooding the nasal passages when making deep dives? If we assume a 2,000-l lung volume and 200-l laryngeal sac volume, both these will be totally collapsed, and all the air will reside in the 100-l nasal passage volume, at a depth of 220 m (see Eq. 7). Echo-sounder records show blue whales diving to near 300 m depth (Alling et al. 1991), so it seems the whale must either flood the nasal passage, allow blood or tissue to fill in the nasal passage, or hold a significant differential pressure. One approach to estimating the minimum differential pressure a blue whale can hold is to estimate the pressure associated with a blow. Using the rise time and rise height to estimate flow velocity and treating the nasal passages as a nozzle in a fluid dynamics calculation yields differential pressures of 1 to 2 bar, not enough to allow diving 80 m below the lung collapse depth (8 bar).

8.3 Gaps in Call Pattern Should Coincide with Surfacing

The presence of pauses between calls and breathing gaps is consistent with the physical model presented here in that a type "B" call could not be produced without a depth change to compress or decompress the lung, thus production of type "B" calls must cease while the whale is at the surface to breath. The pressure required to compress the lung volume into the volume on the narial side of the oscillating valve is too great to expect muscle contraction along to provide, thus requiring the depth-related compression.

8.4 Application to Other Baleen Whale Species

The uniquely long, loud calls of the blue whale require volume displacements greater than any other whale, limiting model applications primarily to the blue whale, although similar methods may be applied to other mysticetes. Humpback whale calls, fin whale calls, and the pulsive type "A" and short duration blue whale calls could all be produced by laryngeal sac contractions alone, the air being recycled between calls or call segments. Table 10.1 lists total volume displacement estimates for a variety of low-frequency whale calls. If no resonance is present, the minimum flow. There appears to be insufficient published data to adequately compare laryngeal sac volumes among species, but Figure 10.22 is a compilation of published data on laryn-

TABLE 10.1. Some parameters of the blue and humpback whales signals

Species and Call Type	Fundamental Frequency (Hz)	Duration (seconds)	Intensity (dB re 1 μPa)	Volume displacement (liters)
humpback	200	4	165	1.5
fin	25–16 swept	0.8	185	35
bowhead	250–100 swept	1.0	165	0.6
blue "A" pulse	17	0.6	182	25
blue "B" call	17	19	185	1,000
blue "D" call	70–30 swept	3	185	50
blue "C" call	10	7	155	25

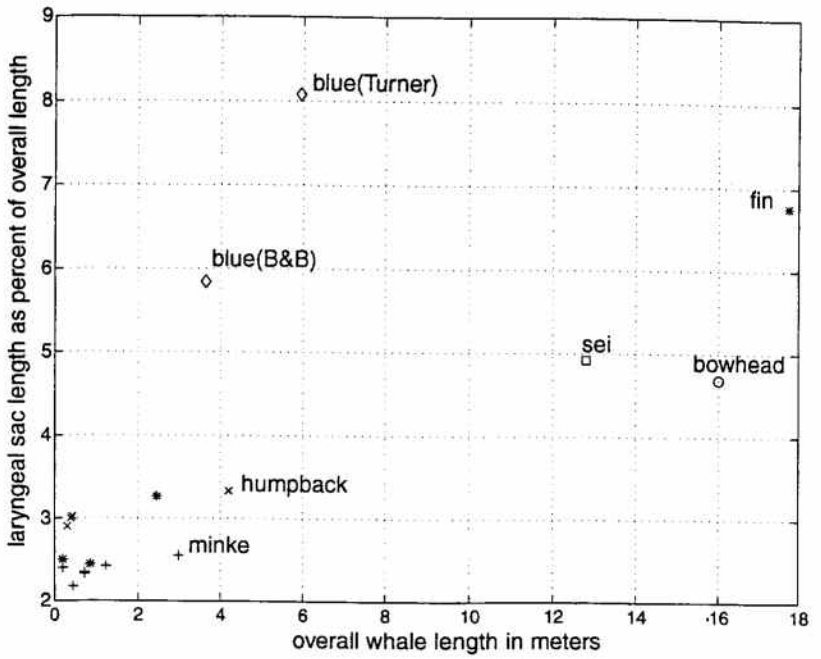

FIGURE 10.22. Laryngeal sac length, defined here as the distance from the ventral tip of the epiglottis to the caudal tip of the laryngeal sac cavity, is plotted as a percentage of total whale length versus total whale length for each specimen. It appears studies on embryos are not useful in estimating relative laryngeal sizes in adult animals. Relative size of the laryngeal sac and nasal passages may help determine the sound production capabilities of each species. Some data points were interpolated from drawings or other measurements when length as by our definition was not provided. (From Turner 1870; Beauregard and Boulart 1882.)

geal sac lengths plotted as a percentage of the whale's length. Many of the data points are unfortunately from embryos (Sukhovskaya and Yablokov 1979) or juveniles, which appear not to be representative of laryngeal development in adult animals. More anatomical data are needed to constrain the volumetric equations presented previously, as well as to address questions of variability between species.

9. Summary

We have presented a new model for sound production by blue whales. Several lines of evidence suggest that the type "B" blue whale call is best represented by monopole source oscillations of an air-filled cavity. Volume displacement requirements based on sound frequency, duration, and intensity suggest that most of the whale's lung capacity is required to produce the loud, low-frequency type "B" calls. A system is proposed to model blue whale sound production, in which air moves between the lungs and the rigid nasal passages while the whale is diving or ascending in the water column. An absolute depth limit for calling of any type occurs when both the lungs and the laryngeal sac have totally collapsed at about 220 m, while the time-averaged depth for producing the type "B" call is required to be around 30 m. The model also predicts that feeding behavior is incompatible with the swim profile and may be incompatible with the requirement that the nasal passages connect to the trachea, possibly blocking the esophagus. The lack of depth-related changes in call characteristics and the anatomy suggest that resonance may be of the Helmholtz type with a low to moderate quality factor (Q). Continued research is expected to provide dive profile information from calling blue whales, testing the proposed model.

Acknowledgments. James Aroyan wishes to thank Whit Au and Joel Kent (Elo TouchSystems, Inc., Fremont, CA) for their insightful comments on his dissertation, and Ted Cranford for providing the CT scan of a common dolphin used in this investigation. The author also thanks Geoffrey Vallis (Geophysical Fluid Dynamics Laboratory, Princeton University) and the UC Santa Cruz Physics department for partial support during the final phase of his doctoral project. James adds a dedication of this chapter to the memory of his father, Harry J. Aroyan (1921–1998).

Help with the mathematics in developing the blue whale sound production model was provided by Ron Kessel. Sue Moore and Kate Stafford expanded our understanding of blue whales through many conversations and their help at sea. John Heyning provided access to the L. A. county museums collections.

Appendix A

This Appendix gives the far-field form of the Helmholtz integral equation used in the modeling of Aroyan (1996) and notes aspects of its numerical implementation. We also illustrate a simple example of a computed far-field pattern and introduce an efficient representation of this data over all emission directions.

It can be shown that the following expression is proportional to the far-field pressure [Eq. (3)] when $R >> \sigma$ [Aroyan (1996)]:

$$p_{ff}(\hat{\mathbf{R}}) = \oint_S \left\{ ik\hat{\mathbf{R}}\cdot\mathbf{n}\,p(\boldsymbol{\sigma}) + \frac{\partial p(\boldsymbol{\sigma})}{\partial n} \right\} e^{-ik\hat{\mathbf{R}}\cdot\boldsymbol{\sigma}} dS(\boldsymbol{\sigma}) \tag{A1}$$

where $\hat{\mathbf{R}} = \mathbf{R}/R$ defines the unit vector in the direction of the far-field point (geometry diagrammed in Figure 10.2). The values of the pressure p and the normal derivative of the pressure $\partial p/\partial n$ over the extrapolation surfaces were obtained from finite difference (FD) simulations. Since both the pressure and the normal derivative fields were obtained by simulation, the difficulties normally associated with nonunique solutions at eigenfrequencies of the interior problem were not encountered. These simulated p and $\partial p/\partial n$ fields were then interpolated with continuous (complex bicubic) polynomials, allowing a high-order approximation to the integral (Eq. A1) to be

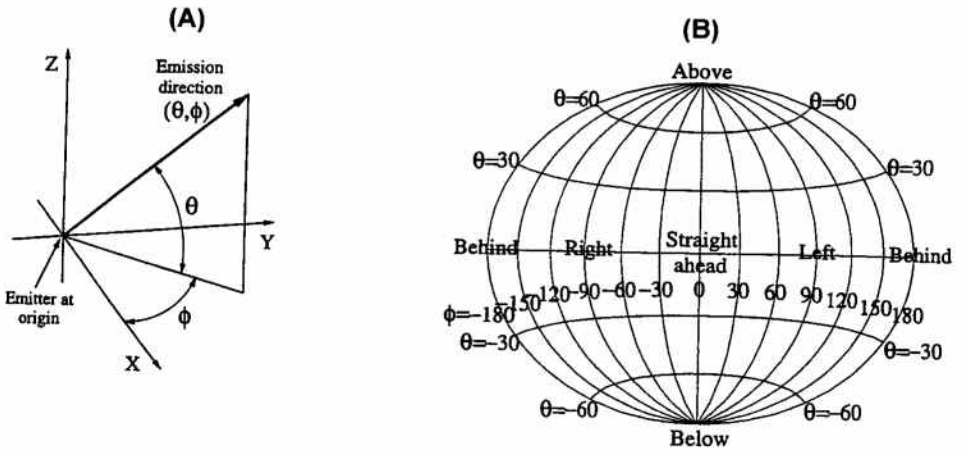

FIGURE 10.A1. Diagrams of the global emission representation used in Figure 10.A2A and in the biosonar emission results of Section 3. (A) defines vertical angle θ and horizontal angle ϕ with respect to the simulation axes directions. Note θ and ϕ are both defined to be zero in the forward direction. (B) diagrams the global equal-area mapping of emission angles θ and ϕ. The viewer orientation may be thought of as looking back at the emitter (center map) from a position forward of the emitter at the unravelled globe of emission directions.

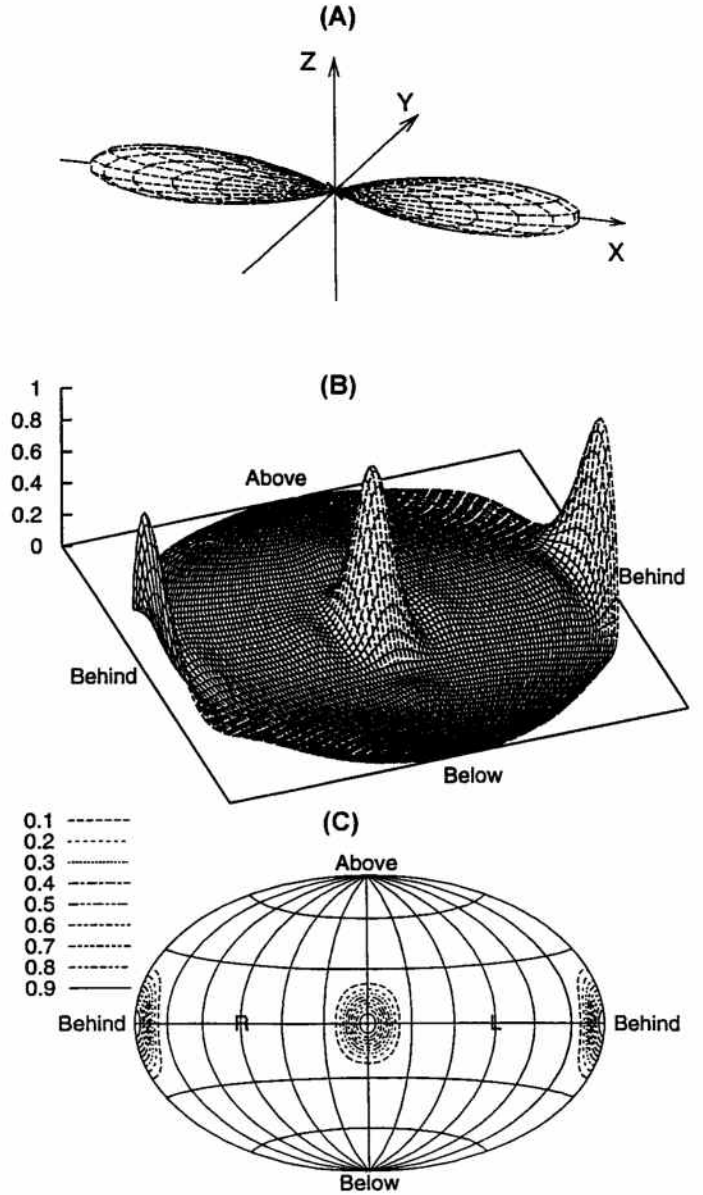

FIGURE 10.A2. (A) Spherical polar plot of the computed far-field emission pattern of a 2-side square pressure sperture (unbaffled and unphased) of side-length 2.0 λ lying in the $x = 0$ plane. The normalized far-field intensity is plotted for 7,200 directions (3° increments in both latitude and longitude). (B) Alternate representation of the same emission data: perspective view of a global mapping of the data with height indicating intensity. (C) Contour plot of the same data projected down into the plane of the global map.

computed over each of the roughly 2×10^5 square subelements of the six faces of the large rectangular extrapolation boxes used in the forward simulations.

Although polar plots of emission data are dramatic, they do not permit rapid examination of the pattern over all spherical angles. For this reason, two alternate ways of visualizing the emission data are utilized in this chapter. These alternate representations make use of the global mapping of emission directions explained in Figure 10.A1.

To familiarize readers with the output of the extrapolation process, Figure 10.A2a illustrates the far-field intensity pattern computed for a 2-sided square pressure aperture (unbaffled and unphased) of side-length 2.0λ lying in the $x = 0$ plane. The surface pressure and normal derivative data over a small $20 \times 40 \times 40$ enclosing box was generated by FD simulation and then input to an extrapolation program. The normalized square magnitude of the far-field pressure computed for 7,200 directions (3° increments in both latitude and longitude) was plotted in spherical polar projection to create the figure. The forward and backward emission lobes produced by this type of aperture are the main features of Figure 10.A2a. A perspective global mapping of this same emission data with height indicating intensity is illustrated in Figure 10.A2b, while Figure 10.A2c is a contour plot of the same data projected down into the plane of the global map. Once understood, these alternative representations provide an excellent means for rapid examination of the far-field data over all angles of emission.

References

Aburto A, Rountry DJ, Danzer JL (1977) Behavioral Response of Blue Whales to Active Sinals. San Diego, CA: Naval Command, Control and Ocean Surveillance Center, RDT&E Division, San Diego. Technical Report 1746.

Albers VM (1965) Underwater Acoustic Handbook II. University Park, PA: The Pennsylvania State University Press.

Alling A, Dorsey EM, Gordan JCD (1991) Blue whales (*Balaenoptera musculus*) off the northeast coast of Sri Lanka: distribution, feeding and individual identification. In: Leatherwood S, Donovan GP (eds) Nairobi: United Nations Mar. Mammal. Tech. Rep. 3, Cetaceans and Cetacean Research in the Indian Ocean Sanctuary, pp. 248–258.

Alling A, Payne R (1988) Song of the Indian Ocean Blue Whale, *Balaenoptera musculus* spp., Unpublished manuscript.

Aroyan JL (1990) Numerical simulation of dolphin echolocation beam formation. M.S. Thesis, University of California, Santa Cruz, CA.

Aroyan JL (1996) Three-dimensional numerical simulation of biosonar signal emission and reception in the common dolphin. Ph.D. Dissertation, University of California, Santa Cruz, CA.

Aroyan JL, Cranford TW, Kent J, Norris KS (1992) Computer modeling of acoustic beam formation in *Delphinus delphis*. J Acoust Soc Am 92:2539–2545.

Au WWL (1980) Echolocation signals of the Atlantic bottlenose dolphin (*Tursiops truncatus*) in open waters. In: Busnel RG, Fish JR (eds) Animal Sonar Systems. New York: Plenum, pp. 251–282.

Au WWL (1993) The Sonar of Dolphins. New York: Springer-Verlag.

Au WWL, Floyd RW, Haun JE (1978) Propagation of Atlantic bottlenose dolphin echolocation signals. J Acoust Soc Am 64:411–422.

Baggeroer AB, Kuperman WA, Mikhalevsky PN (1993) An overview of matched field methods in ocean acoustics. IEEE J Ocean Eng 18:401–424.

Baker BB, Copson ET (1953) The Mathematical Theory of Huygen's Principle, 2nd ed. Oxford: Oxford University Press.

Barham EG (1973) Whales' respiratory volume as a possible resonant receiver for 20 Hz signals. Nature 245:220–221.

Beauregard H, Boulart R (1882) Larynx et la Trachée des Balænides. Journal de l'Anatomie et de la Physiologie Normales et Pathologiques de l'Homme et des Animaux 18:611–634.

Benham WB (1901) On the larynx of certain whales (*Cogia*, *Balænoptera*, and *Ziphius*). Proc Zool Soc London 1:278–300.

Berg RE, Stork DG (1995) The Physics of Sound. Englewood Cliffs, NJ: Prentice-Hall.

Brodie PF (1993) Noise generated by the jaw actions of feeding fin whales. Can J Zool 71:2546–2550.

Cann CE (1988) Quantitative CT for determination of bone mineral density: a review. Radiology 166:509–522.

Carstensen EL (1979) Absorption of sound in tissues. In: Linzer M (ed) Ultrasonic Tissue Characterization II. Washington, DC: US GPO, NBS Special Publication 525, pp. 29–36.

Conner RC (1994) The Lives of Whales and Dolphins. New York: Henry Holt.

Copley LG (1968) Fundamental results concerning integral representations in acoustic radiation. J Acoust Soc Am 44:22–32.

Cranford TW (1992) Functional morphology of the odontocete forehead: implications for sound generation. Ph.D. Dissertation, University of California, Santa Cruz, CA.

Cranford TW, Amundin M, Bain DE (1987) A unified hypothesis for click production in odontocetes. Abstract, seventh Biannual Conf. on Biology of Marine Mammals.

Cranford TW, Amundin M, Norris KS (1996) Functional morphology and homology in the odontocete nasal complex: implications for sound generation. J Morphol 228:223–285.

Cummings WC, Thompson PO (1971) Underwater sounds from the blue whale, *Baleanoptera musculus*. J Acoust Soc Am 50:1193–1198.

Dormer KJ (1979) Mechanism of sound production and air recycling in delphinids: cineradiographic evidence. A Acoust Soc Am 65:229–239.

D'Spain GL, Kuperman WA, Hodgkiss WS, Berger LP (1995) 3-D localization of a blue ography. University of California San Diego, San Diego, California.

Dubrovskiy NA, Zaslavskiy GL (1975) Role of the skull bones in the space-time development of the dolphin echolocation signal. Zool Zh 21:255–258.

Erlichman M (1986) Single photon absorptiometry for measuring bone mineral density. National Center for Health Services Research and Health Care Technology Assessment, US Department of Health and Human Services; NTIS, No. 7.

Evans WE, Sutherland WW, Beil RG (1964) The directional characteristics of delphinid sounds. In: Tavolga WN (ed) Marine Bio-acoustics, Vol. 2. New York: Pergamon, pp. 353–372.

Fletcher NH (1992) Acoustic Systems in Biology. Oxford: Oxford University Press.

Frizzell LA, Carstensen EL, Dyro JF (1976) Shear properties of mammalian tissues at low megahertz frequencies. J Acoust Soc Am 60:1409–1411.

Gilpatrick JW, Perryman WL, Lynn MS (1995) Aaerial photogrammetry and photoidentification of blue whales (*Balaenoptera musculus*) in the California Channel Island—1994. Eleventh Biennial Conference on the Biology of Marine Mammals, Orlando, p. 44.

Goss SA, Johnston RL, Dunn F (1980) Compilation of empirical ultrasonic properties of mamallian tissues, II. J Acoust Soc Am 68:93–108.

Haines G (1974) Sound Underwater. Newton Abbot: David & Charles Ltd.

Haldiman JT, Tarpley (1993) Anatomy and physiology. In: Burns JJ, Montague JJ, Cowles CJ (eds) The Bowhead Whale. Lawrence: The Society for Marine Mammology, pp. 90–97.

Harris GG (1964) Considerations on the physics of sound production by fishes. In: Tavoga WN (ed) Marine BioAcoustics. New York: Pergamon, pp. 233–247.

Henson PW, Ackland T, Fox RA (1987) Tissue density measurement using CT scanning. Australasian Phys Eng Sci Med 10:162–166.

Heyning JE (1989) Comparative facial anatomy of beaked whales (Ziphiidae) and a systematic revision among the families of extant Odontoceti. Los Angeles County Museum, Contr Sci 405:64.

Heyning JE (1995) Masters of the Ocean Realm: Whales, Dolphins, and Porpoises. Vancouver: UBC press.

Hosokawa H (1950) On the cetacean larynx, with special remarks on the laryngeal sack of the sei whale and the aryteno-epiglottideal tube of the sperm whale. Sci Rep Whales Res Inst 3:23–62.

Hunter JA (1988) Dual-energy radiography, dual-photon absorptiometry, and quantitative computed tomography: comparative precision and accuracy in vitro. Ph.D. Dissertation, University of California San Diego, San Diego, CA.

Junger MC, Feit D (1986) Sound, Structures, and Their Interactions, 2nd ed. Cambridge, MA: MIT Press.

Kibblewhite AC, Denham RN, Barnes DJ (1967) Unusual low-frequency signals observed in New Zealand waters. J Acoust Soc Am 41:644–655.

Kinsler LE, Frey AR, Coppens AB, Sanders JV (1982) Fundamentals of Acoustics. New York: John Wiley.

Kroodsma DE (1996) Ecology of passerine song development. In: Kroodsma DE, Miller EH (eds) Ecology and Evolution of Acoustic Communication in Birds. Ithaca, NY: Cornell University Press.

Lee S, Hanson DB, Page EA (1996) Some acoustical properties of the otic bones of a fin whale. J Acoust Soc Am 99:2421–2427.

Lele PP, Sleefe GE (1985) Ultrasonic tissue characterization. In: Repacholi MH, Grandolfo M, Rindi A (eds) Ultrasound—Medical Applications, Biological Effects, and Hazard Potential. New York: Plenum, pp. 343–356.

Lighthill MJ (1978) Waves in Fluids. Cambridge, MA: Cambridge University Press.

Litchfield C, Karol R, Greenberg AJ (1973) Compositional topography of melon lipids in the Atlantic bottlenose dolphin *Tursiops truncatus*: implications for echolocation. Mar Biol 23:165–169.

Litchfield C, Greenberg AJ, Caldwell DK, Caldwell MC, Sipos JC, Ackman RG (1975) Comparative lipid patterns in acoustical and nonacoustical fatty tissues of dolphins, porpoises, and toothed whales. Comp Biochem Physiol 50B: 591–597.

Litchfield C, Karol R, Mullen ME, Dilger JP, Luthi B (1979) Physical factors influencing refraction of the echolocative sound beam in delphinid cetaceans. Mar Biol 52:285–290.

Lockyer C (1981) Growth and energy budgets of large baleen whales from the southern hemisphere. In: Mammals in the Seas. Rome: Food and Agriculture Organization United Nations, pp. 379–487.

Malm, AW (1867) Monographie illustrée de la Baleine trouvée le 29 octobre 1865 . . . (Cited in Beauregard and Boulart), Fol. Stockholm.

Mackay RS, Liaw HM (1981) Dolphin vocalization mechanisms. Science 212: 676–677.

Madsen EL, Sathoff HJ, Zagzebski JA (1983) Ultrasonic shear wave properties of soft tissues and tissuelike materials. J Acoust Soc Am 74:1346–1355.

Malins DC, Varanasi U (1975) Cetacean biosonar: part 2—the biochemistry of lipids in acoustic tissues. In: Malins DC, Sargent JR (eds) Biochemical and Biophysical Perspectives in Marine Biology. New York: Academic, pp. 237–287.

McDonald MA, Hildebrand JA, Webb SC (1995) Blue and fin whales observed on a seafloor array in the Northeast Pacific. J Acoust Soc Am 98:712–721.

Mead JG (1972) Anatomy of the external nasal passages and facial complex in the Delphinidae (Mammalia: Cetacea). Ph.D. Dissertation, University of Chicago, Chicago, IL.

Miles CA (1996) Ultrasonic properties of tendon: velocity, attenuation, and backscattering in equine digital flexor tendons. J Acoust Soc Am 99:3225–3232.

Morris R (1986) The acoustic faculty of dolphins. In: Bryden MM, Harrison R (eds) Research on Dolphins. New York: Clarendon, pp. 369–399.

Morse PM, Ingard KU (1968) Theoretical Acoustics. Princeton, NJ: Princeton University Press.

Norris KS (1968) The evolution of acoustic mechanisms in odontocete cetaceans. In: Drake ET (ed) Evolution and Environment. New Haven, CT: Yale University Press, pp. 297–324.

Norris KS (1980) Peripheral sound processing in odontocetes. In: Busnel RG, Fish JR (eds) Animal Sonar Systems. New York: Plenum, pp. 495–509.

Norris KS, Harvey GW (1974) Sound transmission in the porpoise head. J Acoust Soc Am 56:659.

Northrup JW, Cummings WC, Morrison MF (1971) Underwater 20-Hz signals recorded near Midway Island. J Acoust Soc Am 49:1909–1910.

Omura H, Ichihara T, Kasuya T (1970) Osteology of pygmy blue whale with additional information on external and other characteristics. Sci Rep Whales Res Inst 22:1–27.

Purves PE, Pilleri G (1983) Echolocation in Whales and Dolphins. New York: Academic Press.

Quayle CJ (1991) A dissection of the larynx of a humpback whale calf with a review of its functional morphology. Memoirs of the Queensland Museum 30: 351–354.

Reidenberg JS, Laitman JT (1992) Laryngeal cartilages of the humpback whale (*Megaptera novaeangliae*). Association for Research in Otolaryngology.

Reidenberg JS, Laitman TJ (1993) The silence is broken: role of the cetacean larynx in sound production. American Cetacean Society Fifth Biennial Conference, American Cetacean Society.

Reidenberg JS, Laitman JT (1996) Laryngeal anatomy of the minke whale (*Balaenoptera acutorostrata*): implications for understanding specializations for low frequency sound prouction. Assoc Res Otolaryngol 19:158.

Rivers JA (1997) Blue whale, *Baleanoptera musculus*, vocalizations from the waters off central Calfornia. Mar Mamm Sci 13:186–195.

Romanenko YV (1973) Investigating generation of echolocation pulses in dolphins. Zool Zh 11:1698–1707.

Romanenko YV (1974) On the mechanism of dolphin emission of some pulse and whistle signals. In: Bel'kovich VM, Dubrovskiy NA (eds) (1976) Sensory Bases of Cetacean Orientation. Leningrad: Izdatel'stvo Nauka, pp. 137–148.

Schenck HA (1968) Improved integral formulation for acoustic radiation problems. J Acoust Soc Am 44:41–58.

Seto WW (1971) Acoustics. New York: Mcgraw-Hill.

Seybert AF, Soenarko B, Rizzo FJ, Shippy DJ (1985) An advanced computational method for radiation and scattering of acoustic waves in three dimensions. J Acoust Soc Am 77:362–368.

Stafford KM (1995) Characterization of blue whale calls from the Northeast Pacific and development of a matched filter to locate blue whales on U.S. Navy SOSUS (SOund SUrveillance System) arrays, M.S. Thesis, Oregon State University, Corvallis, OR.

Sukhovskaya LI, Yablokov AV (1979) Morpho-functional characteristics of the larynx in Balaenopteridae. Invest Cetacea 10:205–214.

Thompson PO (1965) Marine Biological Sounds West of San Clemente Island, U.S. Navy Electon. Lab., San Diego, CA.

Thompson PO, Friedl WA (1982) A long term study of low frequency sounds from several species of whales off Oahu, Hawaii. Cetology 45:1–19.

Thompson PO, Findley LT, Vidal O (1992) 20 Hz pulses and other vocalizations of fin whales, *Balaenoptera physalus*, in the Gulf of California, Mexico. J Acoust Soc Am 92:3051–3057.

Tomilin AG (1957) Mammals of the U.S.S.R. and Adjacent Countries. Moscow: Nauka.

True FW (1983) The Whalebone Whales of the Western North Atlantic Compared with those Occuring in European Waters. Washington, DC: Smithsonian.

Turner W (1870) An account of the great finner whale (*Baleanoptera sibbaldi*) stranded at Longniddry. Part 1. The soft parts. Trans R Soc Edinburgh 26:197–251.

Varanasi U, Feldman HR, Malins DC (1975) Molecular basis for formation of lipid sound lens in echolocating cetaceans. Nature 255:340–343.

Varanasi U, Markey D, Malins DC (1982) Role of isovaleroyl lipids in channeling of sound in the porpoise melon. Chem Phys Lipids 31:237–244.

Weston DE, Black RI (1965) Some unusual low-frequency biological noises underwater. Deep-Sea Research 12:295–298.

Wood FG (1964) ••. In: Tavolga WN (ed) Marine Bio-acoustics, Vol. 2. New York: Pergamon, pp. 395–396.

Yablokov AV, Bel'kovich VM, Borisov VI (1972) Whales and Dolphins. Springfield, VA: National Technical Information Service.

Yochem PK, Leatherwood S (1985) Blue whale—*Balaenoptera musculus*. In: Ridgway SH, Harrison RJ (eds) Handbook of Marine Mammals, the Sirenians and Baleen Whales. San Diego: Academic Press.

Zemlin WR (1988) Speech and Hearing Science. Englewood Cliffs, NJ: Prentice-Hall.